

THE HELLAS2XMM SURVEY. VII. THE HARD X-RAY LUMINOSITY FUNCTION OF AGNs UP TO $z = 4$: MORE ABSORBED AGNs AT LOW LUMINOSITIES AND HIGH REDSHIFTS

F. LA FRANCA,¹ F. FIORE,² A. COMASTRI,³ G. C. PEROLA,¹ N. SACCHI,¹ M. BRUSA,⁴ F. COCCHIA,² C. FERUGLIO,²
G. MATT,¹ C. VIGNALI,⁵ N. CARANGELO,⁶ P. CILIEGI,³ A. LAMASTRA,¹ R. MAIOLINO,⁷ M. MIGNOLI,³
S. MOLENDI,⁸ AND S. PUCETTI²

Received 2005 May 16; accepted 2005 August 15

ABSTRACT

We have determined the cosmological evolution of the density of active galactic nuclei (AGNs) and of their N_{H} distribution as a function of the unabsorbed 2–10 keV luminosity up to redshift 4. We used the HELLAS2XMM sample combined with other published catalogs, yielding a total of 508 AGNs. Our best fit is obtained with a luminosity-dependent density evolution (LDDE) model where low-luminosity ($L_{\text{X}} \sim 10^{43}$ ergs s⁻¹) AGNs peak at $z \sim 0.7$, while high-luminosity AGNs ($L_{\text{X}} > 10^{45}$ ergs s⁻¹) peak at $z \sim 2.0$. A pure luminosity evolution model (PLE) can instead be rejected. There is evidence that the fraction of absorbed ($N_{\text{H}} > 10^{22}$ cm⁻²) AGNs decreases with the intrinsic X-ray luminosity and increases with the redshift. Our best-fit solution provides a good fit to the observed counts, the cosmic X-ray background, and to the observed fraction of absorbed AGNs as a function of the flux in the 10^{-15} ergs cm⁻² s⁻¹ $< S_{2-10} < 10^{-10}$ ergs cm⁻² s⁻¹ range. We find that the absorbed, high-luminosity ($L_{\text{X}} > 10^{44}$ ergs s⁻¹) AGNs have a density of 267 deg⁻² at fluxes $S_{2-10} > 10^{-15}$ ergs cm⁻² s⁻¹. Using these results, we estimate a density of supermassive black holes in the local universe of $\rho_{\text{BH}} = 3.2 h_{70}^2 \times 10^5 M_{\odot}$ Mpc⁻³, which is consistent with the recent measurements of the black hole mass function in the local galaxies.

Subject headings: diffuse radiation — galaxies: active — galaxies: evolution — quasars: general — surveys — X-rays: diffuse background

1. INTRODUCTION

The understanding of the history of accretion in the universe and of the formation of massive black holes and their host galaxies relies on the measurement of the space density and evolution of active galactic nuclei (AGNs). According to the AGN unified model (Antonucci 1993) the viewing angle between the observer and the symmetry axis of the nuclear structure is responsible for the different classification. In type 1 AGNs the central engine is directly visible. Both the broad and narrow line emitting regions are detected in the optical spectra along with a soft unabsorbed X-ray spectrum. On the other hand, a type 2 AGN classification arises when the broad-line region and the soft X-rays are obscured by a dusty torus.

Until a few years ago, the best measurements of the cosmological evolution of the AGN luminosity function were essentially limited to optically (e.g., La Franca & Cristiani 1997; Croom et al. 2004) and soft X-ray (e.g., Maccacaro et al. 1991; Miyaji et al. 2000) selected type 1 AGNs. While there is evidence that type 2 AGNs are about a factor of 4 more numerous than type 1 AGNs (e.g., Maiolino & Rieke 1995; Risaliti et al.

1999), their relative space density beyond the local universe is basically unknown. Assuming that the cosmological evolution of type 1 and 2 AGNs is the same, it was possible to simultaneously reproduce the X-ray background spectrum and the X-ray counts (e.g., Setti & Woltjer 1989; Comastri et al. 1995). This simple picture was later slightly modified in models where the fraction of type 2 AGNs was assumed to increase toward higher redshifts (e.g., Pompilio et al. 2000; Gilli et al. 1999, 2001). The selection of complete samples of type 2 AGNs is a difficult task. In the optical they are often so dim that only the light of the host galaxy is visible; at $z > 1$ even the latter usually has $R > 24$. In the soft X-ray bands even hydrogen column densities, N_{H} , of the order of 10^{21} – 10^{22} cm⁻² may strongly suppress the flux. In the hard (2–10 keV) X-rays there is less bias against type 2 AGN selection, although the absorption due to large N_{H} column densities (10^{23} – 10^{24} cm⁻²) is not negligible, especially at low redshifts.

Early attempts to compute the hard X-ray luminosity function, based on *ASCA* (*Advanced Satellite for Cosmology and Astrophysics*; Boyle et al. 1998) and *BeppoSAX* observations (La Franca et al. 2002) indicated a strong evolution for type 1 AGNs, with a rate similar to that measured in soft X-rays. Unfortunately, the low spatial resolution of the X-ray detectors prevented an unambiguous identification of the type 2 AGN optical counterparts, thus hampering a reliable determination of the type 2 AGN space density.

Thanks to the high sensitivity and spatial resolution of the hard X-ray detectors on board *XMM-Newton* and *Chandra*, it has become possible to carry out AGN surveys that are less biased against X-ray absorption and have more secure optical identifications. However, at fluxes fainter than $S_{2-10} \sim 10^{-14}$ ergs cm⁻² s⁻¹, a sizeable fraction of the X-ray sources already have optical magnitudes fainter than the spectroscopic limit of 8–10 m class optical telescopes, and thus the measure of their distance has

¹ Dipartimento di Fisica, Università degli Studi “Roma Tre,” Via della Vasca Navale 84, I-00146 Roma, Italy; lafranca@fis.uniroma3.it.

² INAF, Osservatorio Astronomico di Roma, Via Frascati 33, I-00100 Monteporzio, Italy.

³ INAF, Osservatorio Astronomico di Bologna, Via Ranzani 1, I-40127 Bologna, Italy.

⁴ Max Planck Institut für Extraterrestrische Physik (MPE), Giessenbachstrasse, Postfach 1312, 85741 Garching, Germany.

⁵ Dipartimento di Astronomia, Università di Bologna, Via Ranzani 1, I-40127 Bologna, Italy.

⁶ Università di Milano-Bicocca, Piazza della Scienza 3, I-20126 Milano, Italy.

⁷ INAF, Osservatorio Astrofisico di Arcetri, Largo Fermi 5, I-50125 Firenze, Italy.

⁸ INAF, IASF, Via Bassini 15, I-20133, Milano, Italy.

to rely on photometric redshifts, when it is not impossible altogether.

For these reasons, although the Chandra Deep Field–North (CDF-N; Alexander et al. 2003) and the Chandra Deep Field–South (CDF-S; Giacconi et al. 2002) surveys have resolved a fraction of the 2–10 keV X-ray background (XRB) as large as 85%–90% (see also Brandt & Hasinger 2005), a clear picture of AGN evolution that is able to reproduce the whole set of observational constraints (i.e., soft and hard X-ray counts, X-ray background, and N_{H} and redshift distributions) is still missing.

Attempts to take into account the redshift incompleteness of X-ray–selected AGNs have been carried out by Cowie et al. (2003), Fiore et al. (2003), and Barger et al. (2005) combining data from deep and shallow surveys. They independently demonstrated that the AGN number density for luminosities lower than $\sim 10^{44}$ ergs s^{-1} peaks at a lower redshift than that of high-luminosity objects. Making use of an almost complete sample of 247 AGNs from *Chandra*, *ASCA*, and *HEAO 1* (*High Energy Astronomical Observatory*) surveys above a limiting flux of $S_{2-10} > 3.8 \times 10^{-15}$ ergs cm^{-2} s^{-1} , Ueda et al. (2003) were able to estimate the hard X-ray luminosity function (HXLf) up to $z = 3$. They found that the fraction of X-ray–absorbed AGNs decreases with intrinsic luminosity and that the evolution of the AGN HXLf is best described by a luminosity-dependent density evolution (LDDE). Very similar results were also obtained by Hasinger et al. (2005) using an almost complete sample of soft X-ray–selected type 1 AGNs.

In this paper we expand the study carried out by Fiore et al. (2003) with the aim of computing the shape and evolution of the HXLf and N_{H} distribution of all AGNs with $N_{\text{H}} < 10^{25}$ cm^{-2} up to $z \sim 4$. To reach such a goal it is necessary to cover the widest possible range in $L_{\text{X}}-z-N_{\text{H}}$ space and to take into account all possible selection effects. For these reasons we have used a large AGN sample (about 500 objects) that is 4 times deeper than the Ueda et al. (2003) sample. A new method of correcting for the spectroscopic incompleteness of faint X-ray sources is presented and discussed in detail. The selection effects due to X-ray absorption are also specifically discussed and estimated by an appropriate X-ray “*K*-correction” term.

The paper is structured as follows: in § 2 we describe the adopted X-ray samples, and in § 3 the method of computing the HXLf is discussed. The results are presented in § 4, discussed in § 5, and summarized in § 6.

Throughout this paper we call AGNs all objects with an intrinsic (corrected for N_{H} absorption) 2–10 keV X-ray luminosity larger than 10^{42} ergs s^{-1} . In the last few years evidence for a mismatch between optical (type 1/2) and X-ray (unabsorbed/absorbed) classification has emerged (e.g., Fiore et al. 2000). In this paper we refer to AGN1’s if broad emission lines (rest-frame FWHM > 2000 km s^{-1}) are present, while all remaining objects (with or without narrow emission lines in the optical spectrum) are called AGN2’s. If the rest-frame column density is larger than 10^{22} cm^{-2} , the AGN is classified as *absorbed*. The adopted limit is well above the typical X-ray absorption by host galaxy gas (disk, starburst regions, etc.), thus ensuring that the measured column is most likely related to nuclear obscuration. Unless otherwise stated, all quoted errors are at the 68% confidence level. We assume $H_0 = 70$ km s^{-1} Mpc^{-1} , $\Omega_m = 0.3$, and $\Omega_\Lambda = 0.7$.

2. SAMPLES

In order to cover the widest possible range of luminosities and redshifts, we combined the HELLAS2XMM sample (Fiore et al. 2003) with other existing flux-limited samples, which

TABLE 1
THE SAMPLES

| Sample (1) | Flux Limit (ergs cm^{-2} s^{-1}) (2) | N_{S} (3) | N_{sp} (4) | R_{lim} (5) |
|--------------------------|---|-----------------------|------------------------|-------------------------|
| <i>HEAO 1</i> | 2.9×10^{-11} | 31 | 31 | ... |
| AMSSn..... | 3.0×10^{-13} | 74 | 74 | ... |
| HBS28..... | 2.2×10^{-13} | 27 | 27 | ... |
| H2XMM ^a | 8.0×10^{-15} | 120 | 103 (93) | 23.65 |
| H2XMM ^b | 8.0×10^{-15} | 110 | 44 | 21.40 |
| Lockman..... | 2.6×10^{-15} | 55 | 41 (39) | 23.50 |
| CDF-N..... | 1.0×10^{-15} | 146 | 108 (102) | 24.65 |
| CDF-S..... | 1.0×10^{-15} | 127 | 102 (98) | 25.00 |

NOTES.—Col. (2): flux limit of the samples. Col. (3): total number of sources. Col. (4): number of sources brighter than the spectroscopic limit (in parentheses is the number with redshift). Col. (5): spectroscopic completeness magnitude.

^a 1df sample (Fiore et al. 2003).

^b 0.5df sample (Cocchia et al. 2005).

allowed estimates of the rest-frame N_{H} column density of each AGN. Whenever possible, the column density and the photon index (Γ) were determined with a proper spectral analysis. Otherwise, we assumed $\Gamma = 1.8$ and used the hardness ratio to measure the $z = 0$ column density ($N_{\text{H}0}$; see also the discussion about the uncertainties of this approach in § 4.1.1). The rest-frame column density (N_{H}) was then estimated by the relation $\log N_{\text{H}} = \log N_{\text{H}0} + 2.42 \log(1 + z)$, which makes use of the Morrison & McCammon (1983) cross sections, also including the effects of the absorption edges, and assumes solar abundances from Anders & Grevesse (1989).

For those samples whose optical spectroscopic identifications are incomplete, we chose the optical magnitude limit at which the samples are almost spectroscopically complete. (The incompleteness is 6% in the HELLAS2XMM, Lockman, CDF-N, and CDF-S samples.) In these cases (as the X-ray–optical flux distribution of the sources without redshift is almost the same as that of the spectroscopically identified sources, and the fraction of unidentified sources is small) the sky coverage has been reduced according to the fraction of spectra available. Table 1 contains a summary of the characteristics of each sample. The distribution in $L_{\text{X}}-z$ space of all AGNs from the spectroscopically complete subsamples used in our analysis is shown in Figure 1, while Figure 2 shows their distribution in the $S_{\text{X}}-R$ plane.

2.1. The HELLAS2XMM Sample

We used the HELLAS2XMM 1df (1 degree field) sample (Fiore et al. 2003) plus the recently available extension of 0.5 deg^2 (HELLAS2XMM 0.5df; Cocchia et al. 2005). The HELLAS2XMM 1df sample contains 122 sources, serendipitously detected in five *XMM-Newton* fields with $S_{\text{X}}(2-10 \text{ keV}) > 0.8 \times 10^{-14}$ ergs cm^{-2} s^{-1} . In our analysis we used the fluxes and the column densities measured by X-ray spectral analysis (Perola et al. 2004). Among the 122 sources we discarded one star (object 0537006) and one extended source (object 2690013). For three sources with low signal-to-noise ratios the hardness ratio and redshift were used to estimate the rest-frame N_{H} . In summary, the sample contains 120 sources, 115 optically identified and 95 with measured redshift and optical classification. We restricted our analysis to the sources brighter than $R = 23.65$. Down to this limit 93 of 103 sources have been spectroscopically identified.

The HELLAS2XMM 0.5df sample consists of 110 objects brighter than $S_{\text{X}}(2-10 \text{ keV}) = 8 \times 10^{-15}$ ergs cm^{-2} s^{-1} . Among

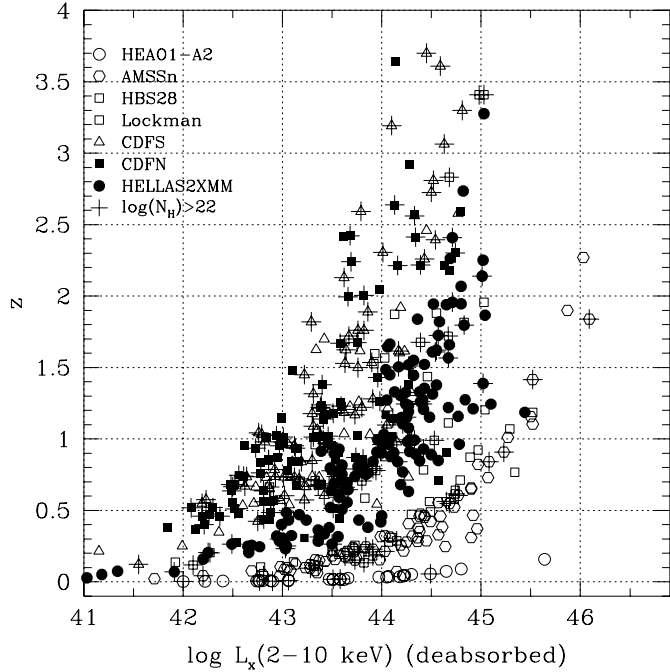


Fig. 1.— L_X - z plane for all AGNs used in this analysis. Different symbols correspond to different surveys, as labeled in the top left corner. Absorbed sources are also highlighted by a cross.

them, 44 sources brighter than $R = 21.4$ (but otherwise randomly selected) have been spectroscopically identified.

2.2. The Piccinotti Sample

The Piccinotti sample is the brightest included in our analysis. It has been obtained through observations carried out by the *HEAO 1* satellite, and it contains 31 sources selected over an area of $26,919 \text{ deg}^2$ down to $S_X(2-10 \text{ keV}) = 2.9 \times 10^{-11} \text{ ergs cm}^{-2} \text{ s}^{-1}$ (Piccinotti et al. 1982). The column densities have been taken from the literature and are derived from X-ray spectral analyses.

2.3. The AMSSn Sample

The AMSSn sample consists of 74 AGNs at fluxes brighter than $S_X(2-10 \text{ keV}) = 3 \times 10^{-13} \text{ ergs cm}^{-2} \text{ s}^{-1}$ (Akiyama et al. 2003). The total area covered is 45 deg^2 at the fainter fluxes and rises to $\sim 69 \text{ deg}^2$ at bright fluxes. The N_H column densities have been derived from the hardness ratios values.

2.4. The HBS28 Sample

The HBS28 sample (Caccianiga et al. 2004) consists of 27 AGNs and 1 star selected in the $4.5-7.5 \text{ keV}$ band. The sources are brighter than $2.2 \times 10^{-13} \text{ ergs cm}^{-2} \text{ s}^{-1}$ (assuming $\Gamma = 1.8$) and have been selected over 82 *XMM-Newton* pointed fields, corresponding to a total of 9.756 deg^2 . All sources have been spectroscopically identified, and their column densities have been measured through X-ray spectral fits.

2.5. The Lockman Hole Sample

The Lockman Hole sample consists of 55 sources selected within the $12'$ radius of the *XMM-Newton* observation. The sources are brighter than $S_X(2-10 \text{ keV}) = 2.6 \times 10^{-15} \text{ ergs cm}^{-2} \text{ s}^{-1}$ (Baldi et al. 2002). Optical identifications and X-ray spectral fits are from Mainieri et al. (2002). Spectroscopic redshifts and classifications have been obtained for 41 objects, while 3 sources have photometric redshifts. We restricted our analysis to the

sources brighter than $R = 23.50$. Down to this limit 39 of 41 sources have been spectroscopically identified.

2.6. The CDF-N Sample

In order to reach almost spectroscopic completeness, we have selected an X-ray-bright subsample in the CDF-N. The subsample consists of 146 sources (see Table 1) selected within the $10'$ radius of the *Chandra* observation (Alexander et al. 2003). The sky coverage reaches $S_X(2-10 \text{ keV}) > 10^{-15} \text{ ergs cm}^{-2} \text{ s}^{-1}$ in the inner $5'.85$ radius, $S_X(2-10 \text{ keV}) > 2.49 \times 10^{-15} \text{ ergs cm}^{-2} \text{ s}^{-1}$ in the annulus between $5'.85$ and $6'.5$ radii, and $S_X(2-10 \text{ keV}) > 3.61 \times 10^{-15} \text{ ergs cm}^{-2} \text{ s}^{-1}$ in the annulus between $6'.5$ and $10'.0$ radii. We used both spectroscopic and spectrophotometric identifications and redshifts available from the literature (Barger et al. 2003). We restricted our analysis to sources brighter than $R = 24.65$. Down to this limit 102 of 108 sources have been spectroscopically identified. The N_H column densities have been derived from the hardness ratios.

2.7. The CDF-S Sample

Although the CDF-S has been observed for 1 Ms instead of the 2 Ms spent in the CDF-N, we selected a spectroscopically complete X-ray-bright subsample with the same sky coverage as for the CDF-N. Indeed, at our adopted flux limits, the difference in the exposure time does not affect the sky coverage. The sample consists of 127 sources (see Table 1; Giacconi et al. 2002; Alexander et al. 2003). We used both spectroscopic and spectrophotometric redshifts available from the literature (Szokoly et al. 2004; Zheng et al. 2004). Moreover, given that both Szokoly et al. (2004) and Zheng et al. (2004) identifications are based on the X-ray source catalog of Giacconi et al. (2002), we have revised some optical/X-ray associations according to the improved astrometry provided by Alexander et al. (2003). We restricted our analysis to sources brighter than $R = 25.00$. Down to this limit 98 of 102 sources have been spectroscopically identified. The N_H column densities have been derived from the hardness ratios.

3. METHOD

We searched for a functional fit to the density of the AGNs as a function of the unabsorbed $2-10 \text{ keV}$ luminosity (L_X), the rest-frame absorbing column density (N_H), and the redshift (z). The method is based on the comparison, through χ^2 estimators, of the observed and expected numbers of AGNs (in L_X - z space) and of the N_H distributions, obtained from computations that take into account all the observational selection effects of the samples.

Once an HXLF evolution model is assumed, the number of expected AGNs (E) in a given bin of the L_X - z - N_H space is the result of the sum, over the number of samples N_{samp} , of the expected number of AGNs in each sample, taking into account the area coverage of each i th sample $\Omega_i(L, N_H, z)$, the N_H distribution $f(L_X, z; N_H)$, and a completeness function $g(L_X, z, N_H, R_i)$, where R_i is the spectroscopic limit of completeness of the i th sample:

$$E = \sum_{i=1}^{N_{\text{samp}}} \iiint \Phi(L_X, z) f(L_X, z; N_H) g(L_X, z, N_H, R_i) \Omega_i(L, N_H, z) \times \frac{dV}{dz} d \log L_X dz dN_H. \quad (1)$$

3.1. The Shape of the Luminosity Function

In order to describe the evolution of the AGNs, we used standard functional forms, such as the pure luminosity evolution

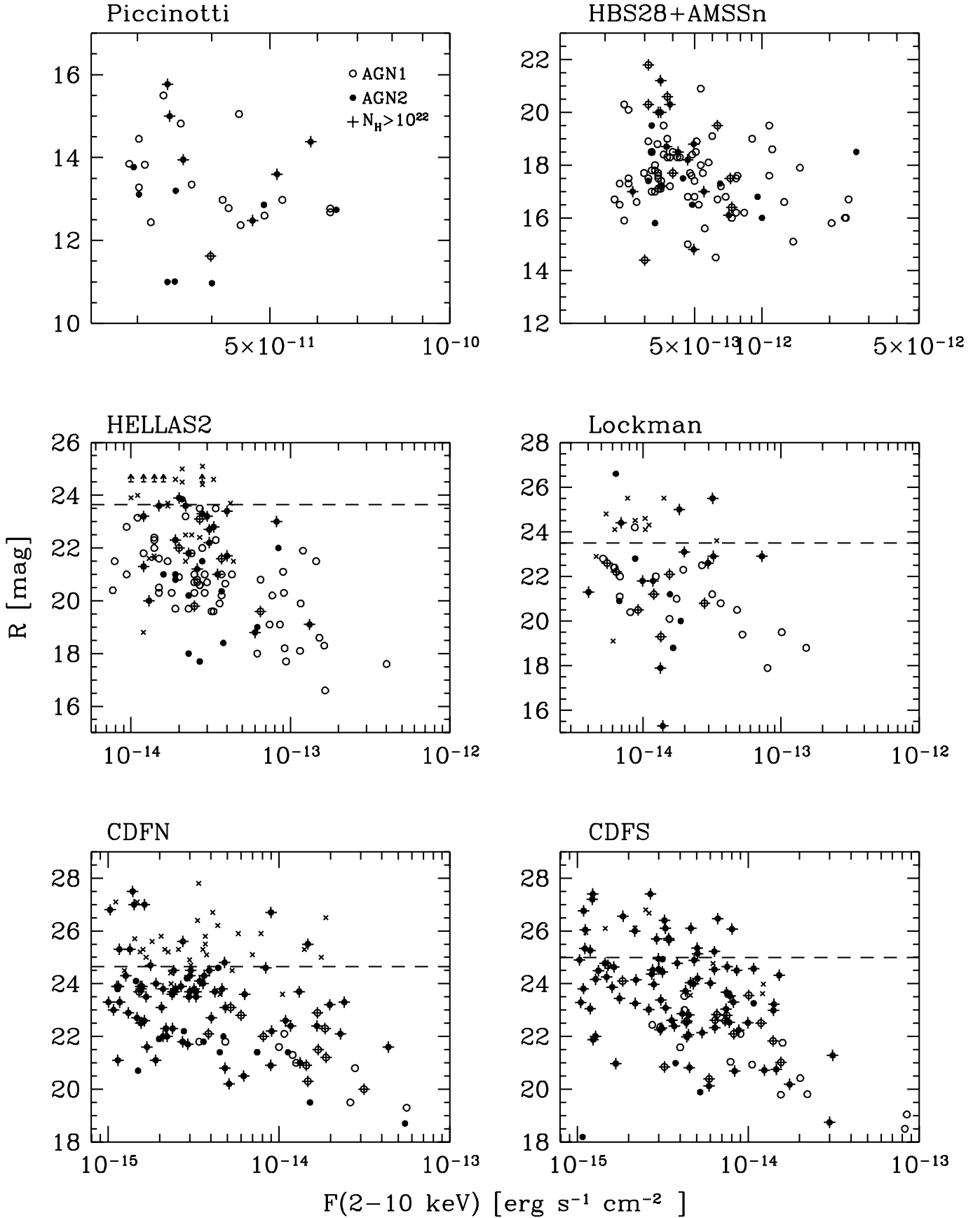


FIG. 2.—*R*-band magnitude vs. 2–10 keV X-ray flux for all sources of the samples used in this analysis. The dashed lines indicate the spectroscopic limits of completeness adopted in our analysis.

(PLE) model and an LDDE model (see next section and, e.g., Boyle et al. 1998; Miyaji et al. 2000; La Franca et al. 2002; Ueda et al. 2003). The HXLF, representing the number density per unit comoving volume and per unit $\log L_X$, as a function of L_X and z , was expressed as

$$\frac{d\Phi(L_X, z)}{d \log L_X}. \quad (2)$$

We adopted a smoothly connected two-power-law form to describe the present-day HXLF,

$$\frac{d\Phi(L_X, z=0)}{d \log L_X} = A \left[\left(\frac{L_X}{L_*} \right)^{\gamma_1} + \left(\frac{L_X}{L_*} \right)^{\gamma_2} \right]^{-1}. \quad (3)$$

3.2. The K -Correction

In order to convert the observed 2–10 keV fluxes (S_X) to the intrinsic 2–10 keV luminosities (L_X) and vice versa, for each observed or “expected” AGN with a given N_H , a K -correction has been computed by assuming a photon index $\Gamma = 1.8$, an exponential cutoff (e^{-E/E_C}) at $E_C = 200$ keV, and the corresponding photoelectric absorption (see § 4.1.1 for a discussion on the use of different K -corrections).

3.3. The Completeness Function

All the faint samples used in our analysis (HELLAS2XMM, Lockmann, CDF-S, and CDF-N) are nearly spectroscopically complete down to a certain optical limiting magnitude ($R = 21.4$ – 25 ; see Table 1). In order to compute the number of expected AGNs in a certain bin of the L_X - z - N_H space, we introduced the completeness function $g(L_X, z, N_H, R)$, which provides the probability that a given AGN with luminosity L_X , redshift z , and column density N_H had an apparent R -band magnitude brighter than the spectroscopic limits of completeness R of each sample.

For this reason we derived an empirical relationship between the unabsorbed X-ray luminosity L_X and the optical luminosity L_R^9 for AGN1’s and AGN2’s and measured their spread (see Fig. 3). For AGN1’s we found

$$\log L_R = (0.959 \pm 0.025) \log L_X + (2.2 \pm 1.1), \quad (4)$$

with a 1σ dispersion of 0.48 (in $\log L_R$ units) around the best-fit solution. The linear correlation coefficient is $r = 0.773$, corresponding to a negligible ($< 10^{-13}$) probability that the data are consistent with the null hypothesis of zero correlation. For AGN2’s a flatter relation was found:

$$\log L_R = (0.462 \pm 0.026) \log L_X + (23.7 \pm 1.1), \quad (5)$$

with a 1σ dispersion of 0.40 (in $\log L_R$ units) and a linear correlation coefficient $r = 0.462$, again corresponding to a negligible ($< 2 \times 10^{-13}$) probability that the data are consistent with the null hypothesis of zero correlation. In order to compute the above relationships, a linear least-squares method with errors (assumed to be 0.2 dex) in both axes has been used. The difference between the two relations should be attributed to the dominance in the optical of the AGN component in the AGN1’s, which produces an almost linear relationship between X-ray and

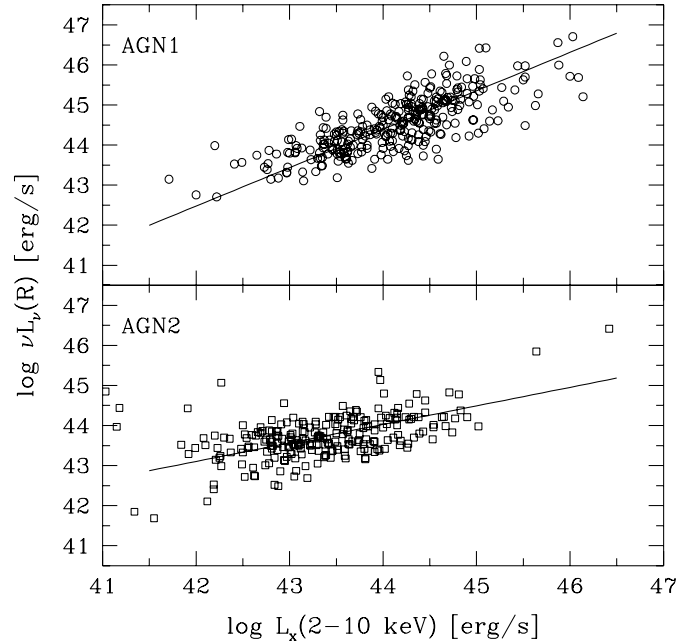


FIG. 3.—The $\log L_X$ – $\log L_R$ relation for optical AGN1’s and AGN2’s. The solid lines correspond to eqs. (4) and (5).

optical luminosity (see La Franca et al. 1995 for similar results in soft X-rays). In AGN2’s, where the nucleus is obscured, the optical luminosity is instead dominated by the host galaxy (see also Fiore et al. 2003).

For each pair of unabsorbed X-ray luminosity and redshift, the above relationships (*with their spreads*) can be used to compute the probability of an AGN appearing brighter than a certain optical magnitude and thus being spectroscopically identified. The observed spreads of the two relationships are due to a combination of the intrinsic spread with the observational uncertainties. Given our aims, both effects should be taken into account, and we have thus not subtracted the contribution of the observational uncertainties from the spread estimates. To choose which L_X - L_R relationship to use (eq. [4] or [5]), we also need to know the probability of an AGN appearing as an AGN1 (or its complement, an AGN2) as a function of L_X , N_H , and z : $Q1(L_X, z, N_H)$. This probability was estimated from the sample itself as described below.

Figure 4 shows the distribution of the observer frame column density N_{H0} as a function of L_X for AGN1’s and AGN2’s in three redshift intervals. Here we do not use the rest-frame N_H but instead the observer frame N_{H0} , which is equivalent to a hardness ratio (see also Hasinger 2003). As can be seen in Figure 5, the probability of finding an AGN1 is dependent not only on N_{H0} but also on the luminosity. The probability of finding an AGN1 increases with increasing luminosity, and there is a relevant fraction of low-luminosity ($L_X < 10^{43}$ ergs s^{-1}) unabsorbed objects that are AGN2’s, while a fraction of the high-luminosity ($L_X > 10^{45}$ ergs s^{-1}) absorbed objects are AGN1’s. This result, if it is not due to contamination by galaxy light in the lower luminosity AGN2’s, contradicts the simplest version of the AGN unified model. The analysis of this issue is beyond the scope of this paper (see Panessa & Bassani 2002; Page et al. 2003; Steffen et al. 2003; Ueda et al. 2003; Brusa et al. 2003; Perola et al. 2004; Barger et al. 2005 for similar results and discussions; see also § 4.6).

As Figure 4 shows, there is no evidence of a dependence on redshift of the distribution of AGN1’s and AGN2’s as a function

⁹ The L_R luminosity is in ergs s^{-1} (νL_ν), computed at 660 nm, where the flux is $f[\text{ergs } s^{-1} \text{ cm}^{-2} \text{ Hz}^{-1}] = 2.84 \times 10^{-20} \times 10^{-0.4R}$ (Zombeck 1990).

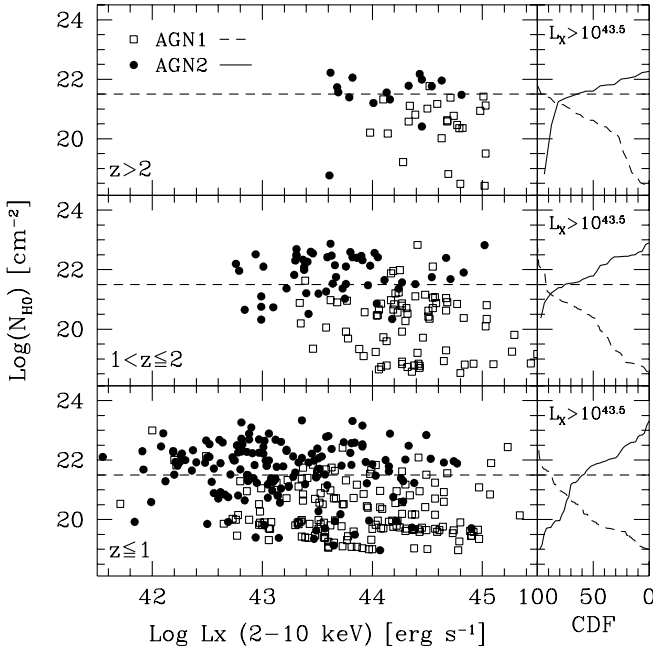


FIG. 4.—The $\log L_X - \log N_{H0}$ plane at $z \leq 1$ (bottom), $1 < z \leq 2$ (middle), and $z > 2$ (top). Open squares represent optical AGN1's; filled circles represent optical AGN2's. On the right side the dashed lines show the cumulative distribution functions of the N_{H0} values for AGN1's with $L_X > 10^{43.5}$ ergs s^{-1} , while the solid lines show the complement of the cumulative distribution function of the N_{H0} values for AGN2's with $L_X > 10^{43.5}$ ergs s^{-1} .

of L_X and N_{H0} . We have thus estimated the probability of an AGN appearing as an AGN1 as a function of L_X and N_{H0} only, by assuming no dependence on redshift. This probability has been estimated as a function of L_X in two bins of N_{H0} ¹⁰: at $N_{H0} \leq 10^{21.5}$ cm^{-2} and $N_{H0} > 10^{21.5}$ cm^{-2} . The values of the probability of an AGN appearing as an AGN1 in these two N_{H0} intervals are shown in Figure 5.

We caution the reader that, due to inhomogeneities in the quality of the spectroscopic classification of the samples used, the above measure of the fraction of AGN1's as a function of L_X and N_{H0} has uncertainties that are difficult to quantify. However, these estimates are only used to derive which fractions of the unidentified AGNs will follow the two $L_X - L_R$ relationships shown in equations (4) and (5). The absence of many outliers in the $L_X - L_R$ relationships for AGN1's and AGN2's shown in Figure 3 demonstrates qualitatively that classification errors should not be very large. This, in principle, does not imply that more accurate spectroscopy would not change the optical classification of the AGNs but that the spectroscopy is accurate enough, for our purposes, to decide which of the two $L_X - L_R$ relationships the AGN would follow. However, the completeness correction is computed under the assumption that the measured fraction of AGN1's as a function of L_X and N_{H0} and the derived two $L_X - L_R$ relationships for AGN1's and AGN2's also hold for the higher redshift, optically fainter, unidentified population. We discuss in § 4 how

¹⁰ Here we chose to use the observed column densities (N_{H0}) instead of the intrinsic ones (N_H) in order to eliminate the dependencies on the redshift. A constant (with z) $N_{H0} = 10^{21.5}$ cm^{-2} separation limit corresponds to a shift of this limit toward higher values of N_H with increasing redshift [as the intrinsic and the $z = 0$ column densities are related by the equation $\log N_H = \log N_{H0} + 2.42 \log(1+z)$]. We revisit this point in the following sections. However, we wish to stress here that the above relationships have been derived only in order to correct the samples for spectroscopic incompleteness and that $N_{H0} = 10^{21.5}$ cm^{-2} should not be construed as the working separation limit between absorbed and unabsorbed AGNs, which (as defined in § 1) instead is $N_H = 10^{22}$ cm^{-2} .

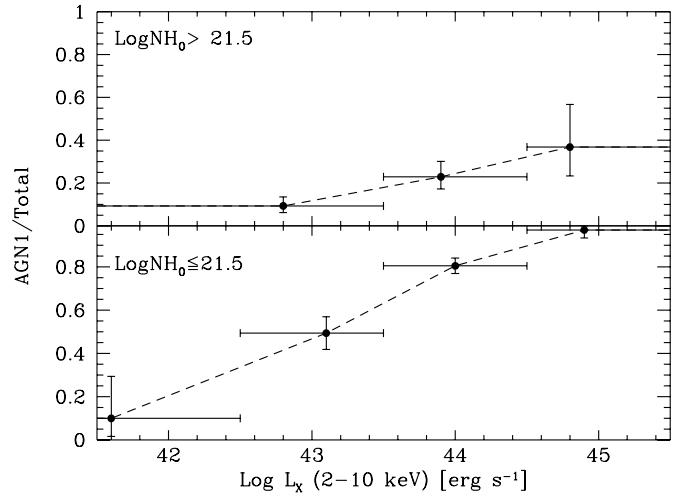


FIG. 5.—Fraction of optical type 1 AGN's with $N_{H0} > 10^{21.5}$ cm^{-2} (top) and $N_{H0} \leq 10^{21.5}$ cm^{-2} (bottom) as a function of the intrinsic luminosity L_X .

much the uncertainties on these assumptions would affect our results.

In summary, the completeness function $g(L_X, z, N_H, R_i)$ was computed as follows: for each given AGN having intrinsic luminosity L_X , redshift z , and absorption column density N_H , (a) N_{H0} was derived according to the equation $\log N_{H0} = \log N_H - 2.42 \log(1+z)$, (b) the probabilities of being an AGN1 (Q1) and AGN2 (1-Q1) were estimated according to the values plotted in Figure 5, and then (c) according to equations (4) and (5) and their spreads, the two probabilities (for the fraction of AGN1's and AGN2's) of being brighter than the spectroscopic limit R_i of the i th sample were computed and summed.

3.4. The N_H Function

To describe the distribution of the spectral parameters of the AGNs at a given luminosity and redshift, we introduced the N_H function, $f(L_X, z; N_H)$, a probability distribution function for the absorption column density as a function of L_X and z . The N_H function (in $\log N_H^{-1}$ units) is normalized to unity at each redshift, over the N_H interval $20 < \log N_H < 25$:

$$\int_{20}^{25} f(L_X, z; N_H) d \log N_H = 1. \quad (6)$$

The objects have been grouped into five bins of N_H , $\Delta \log N_H = 1$ wide, and centered at $\log N_H = 20.5, 21.5, 22.5, 23.5,$ and 24.5 . The first bin includes all the AGNs having $N_H < 10^{21}$ cm^{-2} .

In Figure 6 the observed fraction of absorbed ($N_H > 10^{22}$ cm^{-2}) AGNs as a function of L_X and z is shown. The dotted lines correspond to the fraction of absorbed objects if a flat N_H distribution in the range 10^{20} $cm^{-2} < N_H \leq 10^{25}$ cm^{-2} were assumed, with no selection effects taken into account. The dashed lines show our predictions when these effects are included. Such a model does not provide a good fit to the data points, where a decrease with intrinsic luminosity and an increase with redshift are observed. This behavior is also evident in Figure 7. Bearing in mind that the N_H estimates are affected by uncertainties that can be as large as 1 decade, from the analysis of Figure 7 it appears that the assumption of a flat N_H distribution produces an expected distribution roughly in agreement with the observed one at $N_H > 10^{21}$ cm^{-2} . Hence, the observed change of the fraction of absorbed AGNs as a function of L_X and z (see

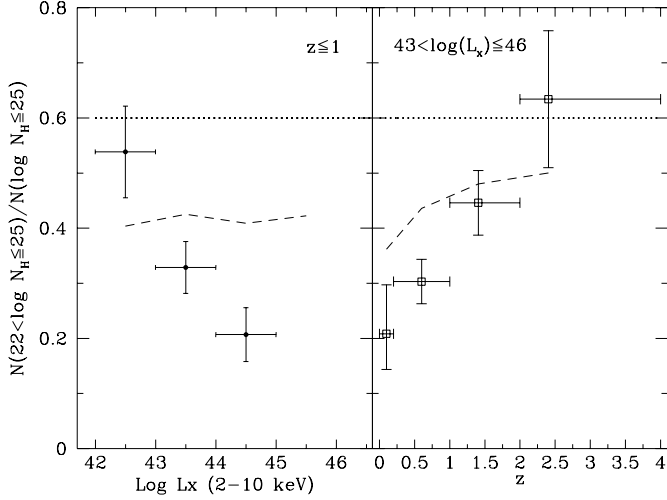


FIG. 6.—Observed fraction of absorbed ($N_{\text{H}} > 10^{22} \text{ cm}^{-2}$) AGNs as a function of L_X (left) and z (right). The dotted lines are the intrinsic fractions assuming a constant flat N_{H} distribution in the range $10^{20} \text{ cm}^{-2} < N_{\text{H}} < 10^{25} \text{ cm}^{-2}$. The dashed lines are the expectations taking into account the selection effects.

Fig. 6) could be mainly attributed to a change of the fraction of AGNs with $N_{\text{H}} < 10^{21} \text{ cm}^{-2}$. This is our working hypothesis, which we analyze in the following sections.

We have thus assumed a flat N_{H} distribution between $N_{\text{H}} = 10^{21}$ and 10^{25} cm^{-2} , while allowing the fraction of objects with $N_{\text{H}} < 10^{21} \text{ cm}^{-2}$ to vary. We introduced a linear dependence of the fraction of objects with $N_{\text{H}} < 10^{21} \text{ cm}^{-2}$ [$\Psi = f(L_X, z; \log N_{\text{H}} < 21)$] on both $\log L_X$ and z :

$$\Psi(L_X, z) = \psi[(\log L_X - 44)\beta_L + 1][(z - 0.5)\beta_z + 1], \quad (7)$$

where ψ is the fraction of objects with $N_{\text{H}} < 10^{21} \text{ cm}^{-2}$ at $L_X = 10^{44} \text{ ergs s}^{-1}$ and $z = 0.5$, and β_L and β_z are the slopes of the linear dependences on L_X and z , respectively. This choice is the simplest possible according to the quality of the data. The function holds for the ranges $0.25 \leq z \leq 2.75$ and $10^{42.5} \text{ ergs s}^{-1} \leq L_X \leq 10^{45.5} \text{ ergs s}^{-1}$. At redshifts and luminosities outside these ranges the fraction was kept constant, equal to the values assumed at the limits of the ranges. Obviously, Ψ could take all values in the range $[0, 1]$. This corresponds to an allowed fraction of absorbed objects ($N_{\text{H}} > 10^{22} \text{ cm}^{-2}$) in the range 0%–75%. Indeed, according to equation (6) and the assumption of a flat N_{H} distribution at $N_{\text{H}} > 10^{21} \text{ cm}^{-2}$, the fraction of absorbed AGNs turns out to be

$$\frac{N(22 < \log N_{\text{H}} \leq 25)}{N(\log N_{\text{H}} \leq 25)} = 0.75(1 - \Psi). \quad (8)$$

As is clear from Figure 7, no object with $N_{\text{H}} > 10^{25} \text{ cm}^{-2}$ is either expected or observed. Thus, we limited our statistical analysis of the evolution of the AGNs to the objects having $N_{\text{H}} \leq 10^{25} \text{ cm}^{-2}$ (see eq. [6]). However, when we predict the number counts, X-ray background, and accretion history (§§ 4.3, 4.4, and 5.2, respectively), we include in the N_{H} distribution a number of objects with $10^{25} \text{ cm}^{-2} < N_{\text{H}} \leq 10^{26} \text{ cm}^{-2}$, equal to that in the interval $10^{24} < N_{\text{H}} \leq 10^{25}$.

3.5. χ^2 Fitting

In order to find the best-fitting model, we choose two χ^2 estimators as figure-of-merit functions. The first estimator (χ_{LF}^2)

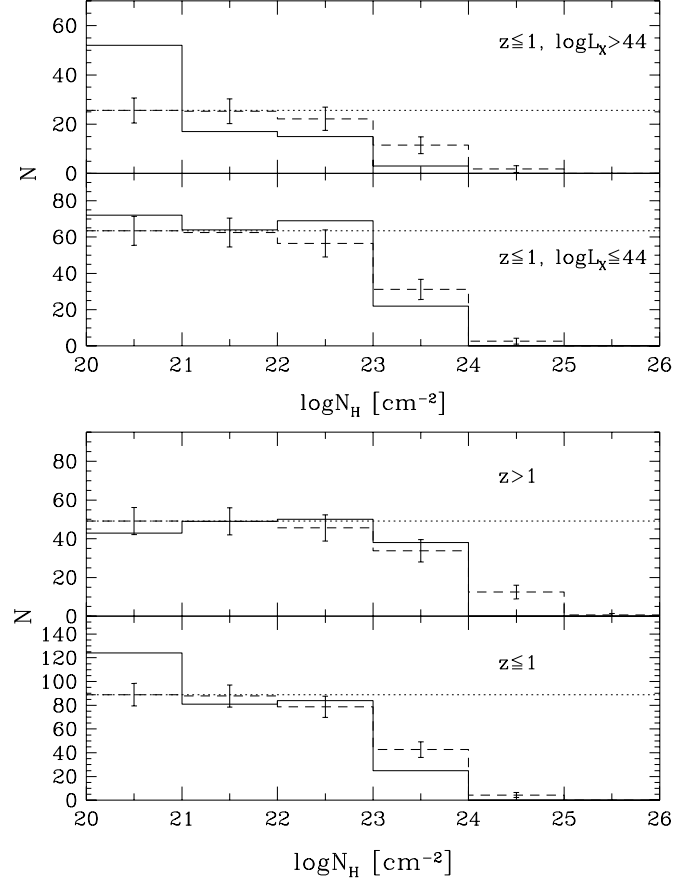


FIG. 7.— N_{H} distributions in various luminosity and redshift intervals. Top: High-luminosity and low-luminosity AGNs at $z < 1$. Bottom: High- and low-redshift AGNs. The solid lines show the observed distributions, the dotted lines show the assumed (constant flat) N_{H} distributions, while the dashed lines show the expectations taking into account the selection effects.

is related to the shape and evolution of the HXLF and is obtained by comparing the expected and observed numbers of AGNs in 24 bins, covering the whole sampled Hubble space (L_X - z ; see Fig. 8 for an example of the binning). Computations have been carried out in the $0 < z < 4.5$ redshift range and in the $10^{42} \text{ ergs s}^{-1} < L_X < 10^{47} \text{ ergs s}^{-1}$ luminosity range. A total of 508 AGNs were used; 190 had N_{H} column densities directly measured from X-ray spectroscopic analysis.

The second estimator ($\chi_{N_{\text{H}}}^2$) is related to the N_{H} function, $f(L_X, z; N_{\text{H}})$, i.e., the shape of the N_{H} distribution and its dependence on L_X and z . One contingency table was created by dividing the objects with column densities higher or lower than $N_{\text{H}} = 10^{22} \text{ cm}^{-2}$ into five further bins in L_X - z space. The $\chi_{N_{\text{H}}}^2$ estimator was computed by comparing the expected and observed number of AGNs in the total 10 (2×5) bins.

The reasons for using two different χ^2 estimators are (1) the number of objects is too small to construct a single χ^2 estimator using bins in the three-dimensional space L_X - z - N_{H} and (2) the two χ^2 estimators cannot be summed, as the data used are not independent. The shape and the evolution of the HXLF are only marginally dependent on the shape and evolution of the N_{H} distribution (we checked that the best-fit parameters of the HXLF vary within the 1σ uncertainties when the parameters of the N_{H} distribution are left to vary within a 3σ range of their best-fit values).

The final fit was obtained by iteratively searching for the lowest values of χ_{LF}^2 and $\chi_{N_{\text{H}}}^2$ in turn, until the changes on the two χ^2

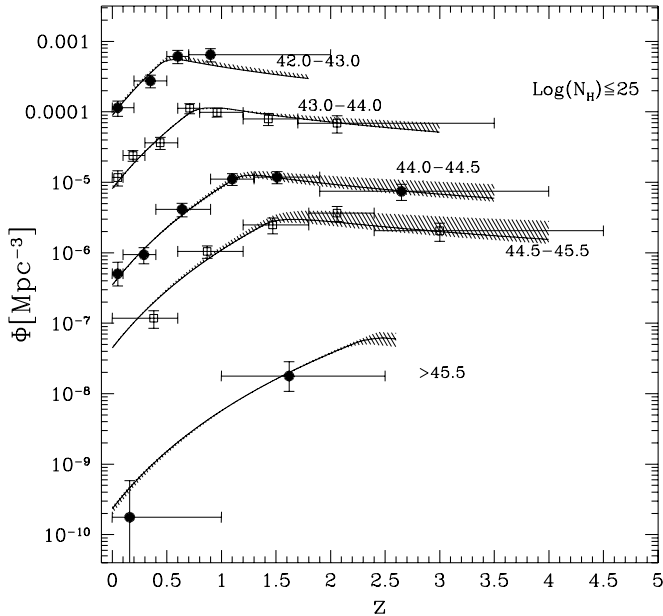


FIG. 8.—Density of AGNs in luminosity bins as a function of redshift. The solid lines show the best-fit values of the LDDE model with an evolving N_H distribution depending on L_X and z (fit 4 in Table 2). Data have been plotted using the $N^{\text{obs}}/N^{\text{mdl}}$ method (see § 4.1). The hatched areas are the largest allowed regions due to uncertainties in the completeness correction method used (see § 4.1.1).

estimators were smaller than 0.1.¹¹ For each model the probabilities for χ^2_{LF} and $\chi^2_{N_H}$, according to the corresponding degrees of freedom, were computed. Confidence regions of each parameter have been obtained by computing $\Delta\chi^2$ at a number of values around the best-fit solution, while leaving the other parameters free to float (see Lampton et al. 1976). The 68% confidence regions quoted correspond to $\Delta\chi^2 = 1.0$. Moreover, in order to perform an unbinned goodness-of-fit test of the HXLF models, we also used a bidimensional Kolmogorov-Smirnov test (2D-KS; Fasano & Franceschini 1987) on the Hubble (L_X - z) space.

4. RESULTS

4.1. The LDDE Model

By introducing the evolution factor

$$e(z) = \begin{cases} (1+z)^{p1}, & z \leq z_c, \\ e(z_c)[(1+z)/(1+z_c)]^{p2}, & z > z_c, \end{cases} \quad (9)$$

the pure density evolution (PDE) model is expressed as

$$\frac{d\Phi(L_X, z)}{d \log L_X} = \frac{d\Phi(L_X, 0)}{d \log L_X} e(z). \quad (10)$$

The z_c parameter represents the redshift at which the evolution stops. The parameter $p1$ characterizes the rate of the evolution, while $p2$ is usually negative and characterizes the rate of the counterevolution of the HXLF at $z > z_c$.

¹¹ This is a small enough interval, as the variance on the χ^2 estimator is $2N_d$, where N_d are the degrees of freedom. Variations of $\Delta\chi^2 = 0.1$ correspond to confidence levels of less than 2% and 3% for χ^2_{LF} and $\chi^2_{N_H}$, respectively.

The LDDE model is obtained by introducing in the PDE model a luminosity dependence of z_c , assumed to be a power law:

$$z_c(L_X) = \begin{cases} z_c^*, & L_X \geq L_a, \\ z_c^*(L_X/L_a)^\alpha, & L_X < L_a. \end{cases} \quad (11)$$

The above parameterization was introduced by Ueda et al. (2003) in order to allow for a change with luminosity of the redshift at which the density of AGNs peaks (see also Miyaji et al. 2000 for a similar LDDE parameterization). This behavior is also apparent in our data (see, e.g., Fig. 8).

In order to plot the HXLF, we adopted the “ $N^{\text{obs}}/N^{\text{mdl}}$ method” (La Franca & Cristiani 1997), where the best-fit model multiplied by the ratio between the number of observed sources and that of the model prediction in each L_X - z bin is plotted. Although model dependent (especially when large bins are used), this technique is the most free from possible biases, compared with other methods such as the conventional $1/V_a$ method. The attached errors are estimated from Poissonian fluctuations (1σ) in the observed number of sources according to the Gehrels (1986) formulae.

We simultaneously fitted the parameters of the HXLF and of the possible dependencies of the N_H distribution on L_X and z . As shown in Table 2, the LDDE model provides a good fit to the data regardless of the adopted N_H distribution (see Figs. 8 and 9).

According to these fits, the redshift of the density peak of AGNs increases with luminosity, from $z \sim 0.5$ at $L_X \sim 10^{42}$ ergs s^{-1} up to $z \sim 2.5$ at $L_X \sim 10^{46}$ ergs s^{-1} . Of the four proposed N_H distributions, only fit 4 provides a good fit to all the data in L_X - z - N_H space. The first model (fit 1) searched for a constant value of the fraction of objects with $N_H < 10^{21}$ cm $^{-2}$ [$\Psi(L_X, z) = \psi = \text{constant}, \beta_L = \beta_z = 0$]. The χ^2 probabilities of the dependence of the N_H distributions on L_X and z reject, at a >99.93% confidence level, this model. As can be seen in Figures 6 and 7, the data require a decrease of the fraction of absorbed objects with luminosity and an increase with redshift. Both N_H distributions in which we allowed for a dependence of the absorbed objects on redshift or luminosity only (fits 2 and 3) are rejected at a >99.5% confidence level. On the other hand, model 4 (Figs. 8 and 9), where a dependence on both redshift and luminosity is allowed (see Figs. 10 and 11), provides a very good representation of the data with a $\chi^2_{N_H}$ probability of 83%.

4.1.1. Analysis of the Uncertainties and Systematic Biases

We analyzed how much our results could be affected by uncertainties in the completeness correction method used. These uncertainties could be introduced by errors in the spectroscopic classification of the AGNs and by the assumption that the measured fraction of AGN1’s as a function of L_X and N_{H0} and the derived two L_X - L_R relationships for AGN1’s and AGN2’s (see § 3.3) also hold for the higher redshift, optically fainter, unidentified population. In order to measure the maximum allowed range of the HXLF parameters due to uncertainties in these assumptions, we have carried out the HXLF fits under the two very extreme hypotheses that all the unidentified AGNs would follow either the L_X - L_R relationship typical of the AGN1’s (eq. [4]) or the L_X - L_R relationship typical of the AGN2’s (eq. [5]). This resulted in the best-fit parameters changing within the measured 1σ uncertainties. The results are shown in Figure 8, where the largest allowed AGN density regions due to the uncertainties introduced by the completeness correction method used are shown by hatched areas.

About 60% of the AGNs used in our analysis have their N_H column densities derived from the hardness ratios (those belonging to the AMSSn, H2XMM0.5, CDF-N, and CDF-S samples).

TABLE 2
2–10 keV AGN LF PARAMETERS

| Model | A^a | p_1 | p_2 | z_{cut} | α | $\log L_a$ (ergs s $^{-1}$) | $\log L^*$ (ergs s $^{-1}$) | γ_1 | γ_2 | ψ | β_L | β_z | $P_{\text{LF}}(\chi^2)^b$ (%) | $P_{\text{LF}}(\text{KS})^b$ (%) | $P_{N_{\text{H}}}(\chi^2)^b$ (%) | XRB_{2-10}^c |
|---------------------------|-------|----------------|----------------|------------------|----------------|---------------------------------|---------------------------------|----------------|----------------|----------------|----------------|----------------|----------------------------------|-------------------------------------|-------------------------------------|-----------------------|
| LDDE | | | | | | | | | | | | | | | | |
| 1..... | 1.48 | 4.37 | -1.19 | 2.39 | 0.20 | 45.74 | 44.26 | 0.94 | 2.35 | 0.26 | 0.00 | -0.00 | 20 | 6 | 0.07 | 1.76 |
| 2..... | 1.50 | 4.39 | -1.14 | 2.41 | 0.20 | 45.74 | 44.25 | 0.97 | 2.36 | 0.29 | 0.43 | -0.00 | 20 | 6 | 0.5 | 1.78 |
| 3..... | 1.39 | 4.48 | -1.19 | 2.39 | 0.20 | 45.74 | 44.26 | 0.94 | 2.35 | 0.30 | 0.00 | -0.33 | 19 | 5 | 0.09 | 1.75 |
| 4..... | 1.21 | 4.62 | -1.15 | 2.49 | 0.20 | 45.74 | 44.25 | 1.01 | 2.38 | 0.44 | 0.62 | -0.51 | 20 | 7 | 83 | 1.81 |
| 5 ^d | 1.29 | 4.85 | -1.03 | 2.45 | 0.22 | 45.73 | 44.23 | 1.09 | 2.44 | 0.36 | 0.67 | -0.00 | 33 | 21 | 20 | 2.16 |
| Errors ^e | 5% | +0.26 -0.26 | +0.72 -0.68 | +0.82 -0.68 | +0.04 -0.03 | +0.58 -0.63 | +0.18 -0.18 | +0.08 -0.10 | +0.27 -0.11 | +0.04 -0.05 | +0.14 -0.13 | +0.14 -0.17 | | | | |
| PLE | | | | | | | | | | | | | | | | |
| 6..... | 6.18 | 3.22 | ... | 1.08 | ... | ... | 43.79 | 0.95 | 2.74 | 0.46 | 0.64 | -0.58 | 9 | 3 | 63 | 2.54 |
| Errors ^e | 5% | +0.13 -0.26 | ... | +0.08 -0.06 | ... | ... | +0.15 -0.11 | +0.06 -0.07 | +0.27 -0.23 | +0.04 -0.05 | +0.14 -0.13 | +0.14 -0.17 | | | | |

^a In units of $10^{-6} h_{70}^3 \text{ Mpc}^{-3}$.

^b Probability values.

^c In units of $10^{-11} \text{ ergs cm}^{-2} \text{ s}^{-1} \text{ deg}^{-2}$.

^d Only Piccinotti, AMSSn, and CDF-N samples used.

^e Errors apply to all models in that section.

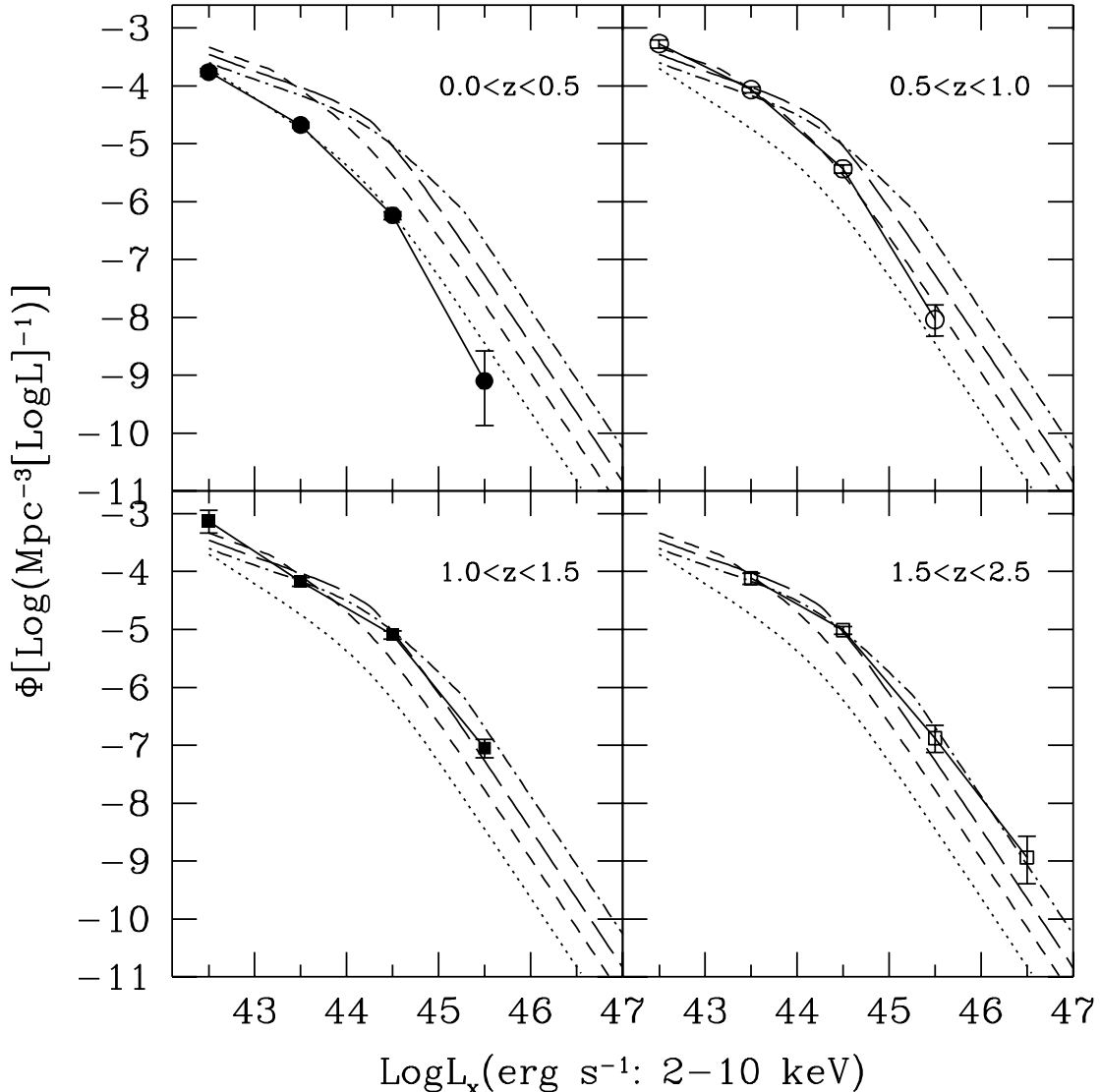


FIG. 9.—Density of AGNs as a function of luminosity in four redshift intervals. The values are plotted at the central redshift of the intervals. The dashed lines show the best-fit densities of the LDDE model with an evolving N_{H} distribution depending on L_{X} and z (fit 4 in Table 2). Data have been plotted using the $N_{\text{H}}^{\text{obs}}/N_{\text{H}}^{\text{mdl}}$ method (see § 4.1).

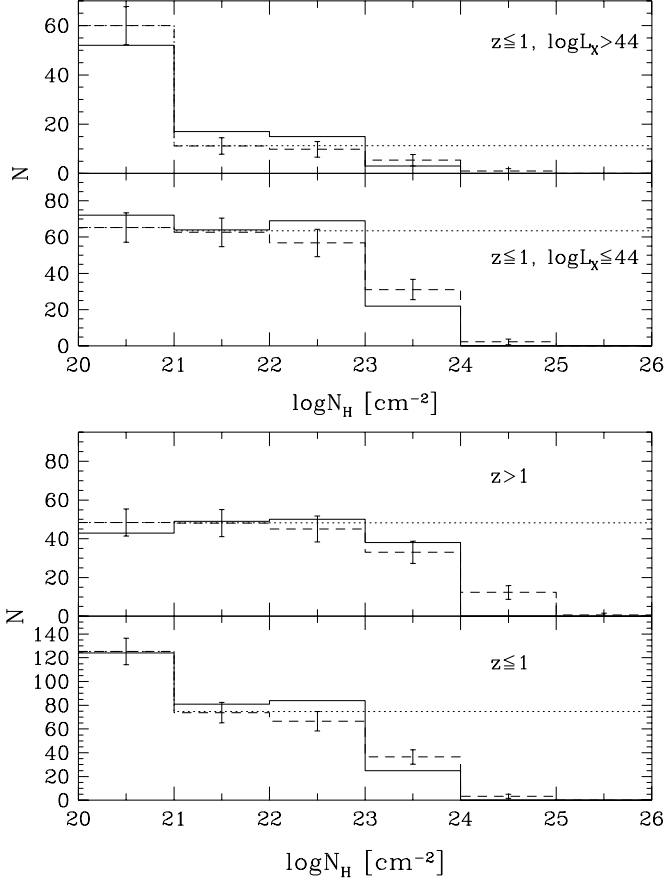


FIG. 10.—Same as Fig. 7, but for the N_{H} distributions of fit 4 in Table 2: evolving N_{H} distribution with an LDDE HXLF evolution.

This method could introduce some systematic bias. For example, our simple absorbed power law model could tendentially underestimate the real column densities because scattered X-rays and circumnuclear starburst X-rays can provide additional flux. This effect is expected to be stronger at lower luminosities, where the fraction of the light coming directly from the nucleus should be smaller. If this is the case, the observed decrease of the fraction of absorbed AGNs with intrinsic luminosity should be even stronger. It should be noted, however, that Perola et al. (2004) found a rather satisfactory correlation between the column densities measured from the hardness ratios and from the X-ray spectral fits in the HELLAS2XMM sample.

Recently, Tozzi et al. (2005) published N_{H} measurements on the CDF-S sample, obtained using X-ray spectral fits. We took advantage of these measures to check whether the hardness ratio method introduces some relevant systematic bias. No relevant difference or systematic trend in either luminosity or redshift was found. In a subsample of $z \leq 1.2$ AGNs, using the hardness ratios we measure a fraction of 17 of 32 absorbed AGNs with $L_X > 10^{43}$ ergs s^{-1} , while Tozzi et al. (2005) find 16 of 32. At lower luminosities (10^{41} ergs $\text{s}^{-1} < L_X \leq 10^{43}$ ergs s^{-1}) we measure a fraction of 20 of 31 absorbed AGNs ($L_X > 10^{43}$), while Tozzi et al. (2005) find 18 of 31. In a subsample with 10^{43} ergs $\text{s}^{-1} < L_X \leq 10^{45}$ ergs s^{-1} at redshift below 1.5 we measure a fraction 23 of 43 absorbed AGNs, while Tozzi et al. (2005) find 24 of 43. At redshift above 1.5 we find a fraction 31 of 43 absorbed AGNs, while Tozzi et al. (2005) find 34 of 43.

We also checked whether our results might depend on the assumed X-ray K -correction (see § 3.2). We repeated fit 4 assuming $\Gamma = 1.7$ or 1.9, or assuming an exponential cutoff at

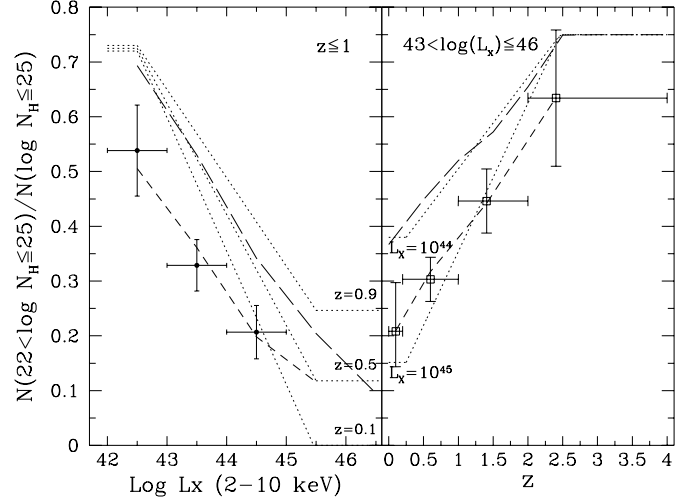


FIG. 11.—Observed fraction of absorbed ($N_{\text{H}} > 10^{22}$ cm^{-2}) AGNs as a function of L_X and z . The dotted lines show examples of the intrinsic assumed distributions at various luminosities and redshifts (LDDE model, fit 4 in Table 2). The long-dashed lines show the corresponding average intrinsic assumed distributions of the sample used. The short-dashed lines show the expectations taking into account the selection effects.

energy $E_C = 300$ keV. It turned out that the changes of the parameters were within the 1σ uncertainties.

4.2. PLE Model

We also checked whether a simpler pure luminosity evolution model was consistent with the data. By introducing the evolution factor

$$e(z) = \begin{cases} (1+z)^{p_1}, & z \leq z_c, \\ e(z_c), & z > z_c, \end{cases} \quad (12)$$

the PLE model is expressed as

$$\frac{d\Phi(L_X, z)}{d \log L_X} = \frac{d\Phi(L_X/e(z), 0)}{d \log L_X}. \quad (13)$$

The PLE fit (Fig. 12 and fit 6 in Table 2) provides a less probable solution for the HXLF. Furthermore, the PLE fit finds that the evolution stops at $z_c = 1.08^{+0.08}_{-0.06}$. This low value should be attributed to the fact that there is an increase with luminosity of the redshift peak of the density of AGNs. Low-luminosity ($L_X < 10^{43}$ ergs s^{-1}) AGNs peak at $z = 0.5$, while high-luminosity ($L_X > 10^{46}$ ergs s^{-1}) AGNs peak at $z \sim 2$. In this framework the PLE fit finds a *weighted mean* of the different redshift cutoff values of the low- and high-luminosity AGNs.

Although formally acceptable, $z_c = 1.08^{+0.08}_{-0.06}$ is significantly smaller than the previous estimates for the evolution of AGN1's in hard X-rays ($z_c = 2.4 \pm 0.5$; La Franca et al. 2002) and in the optical band ($z_c \sim 2.0$; see, e.g., Boyle et al. 2000). This difference should be attributed to the fact that both the hard X-ray AGN1's and the optical QSOs preferentially populate the bright part of the HXLF (see, e.g., Fig. 5 and related discussion), which, also in the LDDE model, faces a redshift cutoff larger than 1.5–2. If the fit of the PLE model is carried out with a fixed $z_c = 2.0$, it turns out to be unacceptable, with a χ^2_{LF} probability of $3.4 \times 10^{-6}\%$ and a 2D-KS probability of 0.27%. On the basis of these results and the fact that the PLE model overpredicts the

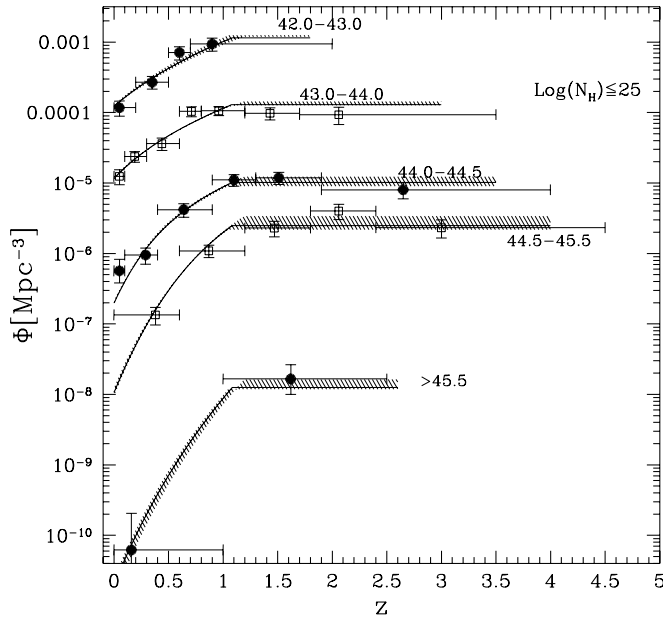


FIG. 12.—Same as Fig. 8, but with the solid lines representing the best-fit values of the PLE model with an evolving N_H distribution (fit 7 in Table 2).

2–10 keV XRB (see Table 2) and the soft X-ray counts (see § 4.3), we rule out such a parameterization of the HXLF evolution.

4.3. The Counts

Down to the flux limit adopted in this analysis (10^{-15} ergs cm^{-2} s^{-1}), the 2–10 keV counts predicted by the models described in Table 2 are in good agreement both with the counts of the whole sample (including the objects without spectroscopic identifications) and with the Bauer et al. (2004) compilation (see Fig. 13). The fit of Moretti et al. (2003) is also shown. This is an a posteriori test implying that our method, used to correct for the

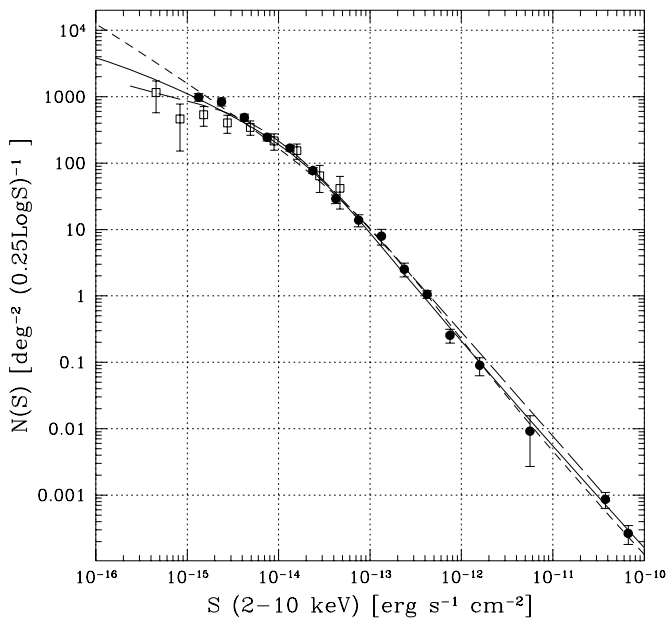


FIG. 13.—Differential counts of AGNs in the 2–10 keV band. The filled circles represent our estimates from the samples used in this analysis. The open squares represent the estimates from Bauer et al. (2004). The solid line shows the counts predicted by the LDDE model (fit 4), while the short-dashed line shows the counts of the PLE model (fit 6). The long-dashed line shows the estimates from a compilation of Moretti et al. (2003).

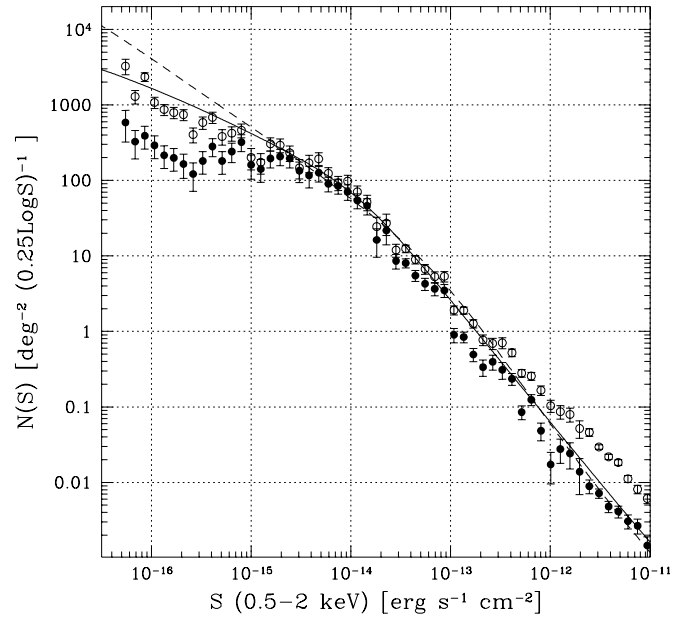


FIG. 14.—Differential counts of X-ray sources in the 0.5–2 keV band (*open squares*) and of AGN1's (*filled squares*) from a compilation of Hasinger et al. (2005). The solid line shows the counts predicted by the LDDE model (fit 4), while the dashed line shows the counts of the PLE model (fit 6).

spectroscopic incompleteness of the faint samples, is reliable. At faint fluxes ($S < 10^{-15}$ ergs cm^{-2} s^{-1} , where there are no data in our samples) the LDDE model is consistent within the errors with the data, while the PLE model tends to overpredict the measured number density.¹² This is mainly due to a higher density of low-luminosity AGNs in the HXLF (in comparison with the LDDE model) and to the absence of a counterevolution at high redshift in the PLE model.

Although this analysis is based on observations made in the 2–10 keV band, it is instructive to compare our results with the 0.5–2 keV counts. Of course, we should be aware that, when predicting the 0.5–2 keV counts, our results depend on the spectral assumptions (a $\Gamma = 1.8$ spectral slope plus photoelectric absorption), which could not be valid below 2 keV. The PLE model overpredicts the observed soft counts as compiled by Hasinger et al. (2005) at faint ($S < 10^{-15}$ ergs cm^{-2} s^{-1}) fluxes (see Fig. 14). The situation is even worse, since at faint fluxes we expect a relevant contribution from normal X-ray galaxies to the counts (about 20 and 400 deg^{-2} at $S_{0.5-2} = 10^{-15}$ and 10^{-16} ergs cm^{-2} s^{-1} , respectively; Ranalli et al. 2003; Bauer et al. 2004). On the other hand, the LDDE model provides a more acceptable solution. At high fluxes the observed counts are above our predictions because the X-ray sources are dominated by stars and clusters of galaxies, which are not included in our models.

4.3.1. The Density of Absorbed AGNs

The 2–10 keV predicted counts obtained from the best-fit model for the HXLF (fit 4) are shown in Figure 15, after being split according to X-ray absorption and X-ray luminosity. Most of the luminous ($L_X > 10^{44}$ ergs s^{-1}), absorbed ($N_H > 10^{22}$ cm^{-2}) sources are AGN2's (see also the discussion in § 3.3). Luminous, obscured AGNs are usually referred to as QSO2's and in the simplest version of the AGN unified scheme are predicted to

¹² As explained in § 3.4, we have included in the N_H distribution a fraction of objects with $10^{25} \text{ cm}^{-2} < N_H \leq 10^{26} \text{ cm}^{-2}$, equal to that in the interval $10^{24} \text{ cm}^{-2} < N_H \leq 10^{25} \text{ cm}^{-2}$.

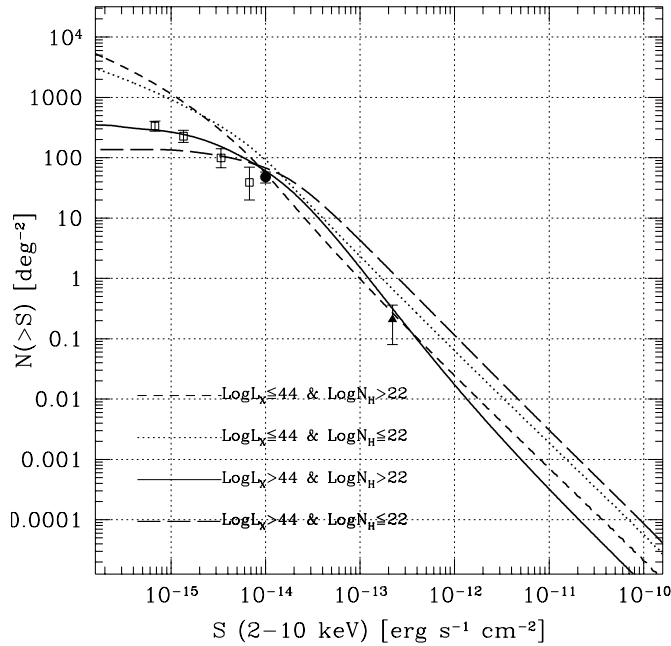


FIG. 15.—Predicted counts (from our best-fit LDDE model 4) of AGNs for unabsorbed and absorbed AGNs divided into two luminosity classes. The filled circle shows the measurement of the density of QSO2’s by Perola et al. (2004), the open squares show the density of QSO2’s derived by Padovani et al. (2004), while the triangle shows the measurement of the density of QSO2’s from the HBS28 sample of Caccianiga et al. (2004).

be more numerous than QSO1’s by a factor comparable to that observed for lower luminosity Seyfert galaxies (about 3–4). Despite extensive searches, narrow-line optically luminous QSO2’s appear to be extremely rare and by far less numerous than broad-line quasars (see Halpern et al. 1998 and references therein). Because of the selection effects due to obscuration, X-ray surveys are expected to provide an unbiased census of the QSO2 population and a more reliable estimate of their space density. Several QSO2 candidates (i.e., luminous, X-ray–obscured sources) have been discovered by *Chandra* and *XMM-Newton* surveys (~ 20 in the HELLAS2XMM survey [Fiore et al. 2003; Mignoli et al. 2004; Cocchia et al. 2005]; ~ 30 in the CDF-S+CDF-N; a dozen in the CLASXS [*Chandra* Large Area Synoptic X-Ray Survey; Barger et al. 2005]). A sizable fraction of them (from 50% to 75%) has been confirmed by deep optical spectroscopic observations. A notable example has been reported by Norman et al. (2002). It should be noted that the quality of spectroscopic observations is not uniform and, given the relatively high redshifts, the $H\alpha$ and $H\beta$ wavelengths are poorly sampled, thus hampering a “pure” optical classification. On the other hand, it is important to recall that the QSO2 classification is wavelength dependent. Several X-ray–obscured, luminous QSO2’s do not show any evidence of strong emission lines even in high-quality optical spectra, among them the QSO2 prototype NGC 6240 (Vignati et al. 1999). Keeping in mind these caveats and adopting an admittedly arbitrary luminosity threshold ($L_X > 10^{44}$ ergs s^{-1}), we obtain a QSO2 space density of 60 and 267 deg^{-2} at 2–10 keV fluxes brighter than 10^{-14} and 10^{-15} ergs $\text{cm}^{-2} \text{s}^{-1}$, respectively. The slope of the integral counts significantly flattens below 10^{-14} ergs $\text{cm}^{-2} \text{s}^{-1}$. As a consequence, the QSO2 surface density at fluxes much fainter than those actually probed (i.e., 10^{-16} ergs $\text{cm}^{-2} \text{s}^{-1}$) increases by a relatively small amount reaching 354 deg^{-2} . These figures have at least a 5% error, corresponding to the HXLF normalization uncertainties. The predicted counts (Fig. 15) are in good agreement with the QSO2

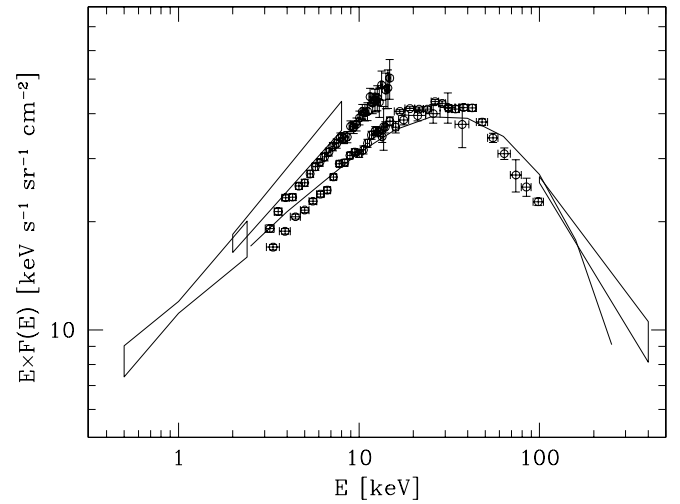


FIG. 16.—Integrated AGN spectrum computed from the best-fit LDDE model for the HXLF (fit 4) with the redshift- and luminosity-dependent N_H function. The model predictions are compared with a selection of XRB spectral measurements over the broad 0.5–400 keV energy range. The regions enclosed within the bow ties correspond to the XRB spectrum and associated errors as measured by *ROSAT* (*Röntgensatellit*; Georgantopoulos et al. 1996) in the 0.5–2 keV band and by *XMM-Newton* (De Luca & Molendi 2004) in the 2–8 keV band. The data points in the 3–15 keV energy range are from *RXTE* (*Rossi X-Ray Timing Explorer*; Revnivtsev et al. 2003), while those in the 3–60 keV are from *HEAO 1 A2* (Marshall et al. 1980). The bow tie at high energies (100–400 keV) is from *HEAO 1 A4* (Kinzer et al. 1997).

space densities measured by Caccianiga et al. (2004), Perola et al. (2004), and Padovani et al. (2004).

4.4. The XRB Spectrum: A Self-Consistency Check

A detailed modeling of the XRB spectrum over the full ~ 2 –400 keV range is beyond the scope of this paper. Nevertheless, it is important to check that the evolving X-ray luminosity function and the N_H distribution derived in the previous sections match the XRB flux at least in the 2–10 keV energy range. To this end it is useful to recall that the XRB intensity below ~ 10 keV, as measured by several imaging X-ray telescopes, is likely to be affected by systematic errors. In Figure 16 a compilation of XRB measurements is reported. The maximum difference is of the order of 30% between the EPIC pn flux reported by De Luca & Molendi (2004) and the *HEAO 1 A2* measure of Marshall et al. (1980). According to a recent reanalysis of the *HEAO 1 A2* data (Revnivtsev et al. 2005) the 3–60 keV spectrum should be renormalized upward by about 15%. The resulting 2–10 keV flux is 1.96 ± 0.10 ergs $\text{cm}^{-2} \text{s}^{-1} \text{deg}^{-2}$. The solid curve in Figure 16 represents the integrated AGN spectrum obtained with our best-fit LDDE model for the HXLF (fit 4) with the redshift- and luminosity-dependent N_H function.¹³ Our predicted 2–10 keV flux of 1.81×10^{-11} ergs $\text{cm}^{-2} \text{s}^{-1} \text{deg}^{-2}$ corresponds to $\sim 92\%$ of the Revnivtsev et al. (2005) value and 108% of the original *HEAO 1 A2* measure. Given that the XRB synthesis has been obtained with very simple prescriptions for the intrinsic (before absorption) spectral energy distribution (a power-law spectrum with $\Gamma = 1.8$ plus an exponential high-energy cutoff e^{-E/E_C} with $E_C = 200$ keV for all AGNs), it is reassuring to obtain a reasonably good description of the XRB spectral intensity over a broad energy range. As a final remark,

¹³ As explained in § 3.4, we have included in the N_H distribution a fraction of objects with $10^{25} \text{ cm}^{-2} < N_H \leq 10^{26} \text{ cm}^{-2}$, equal to that in the interval $10^{24} \text{ cm}^{-2} < N_H \leq 10^{25} \text{ cm}^{-2}$.

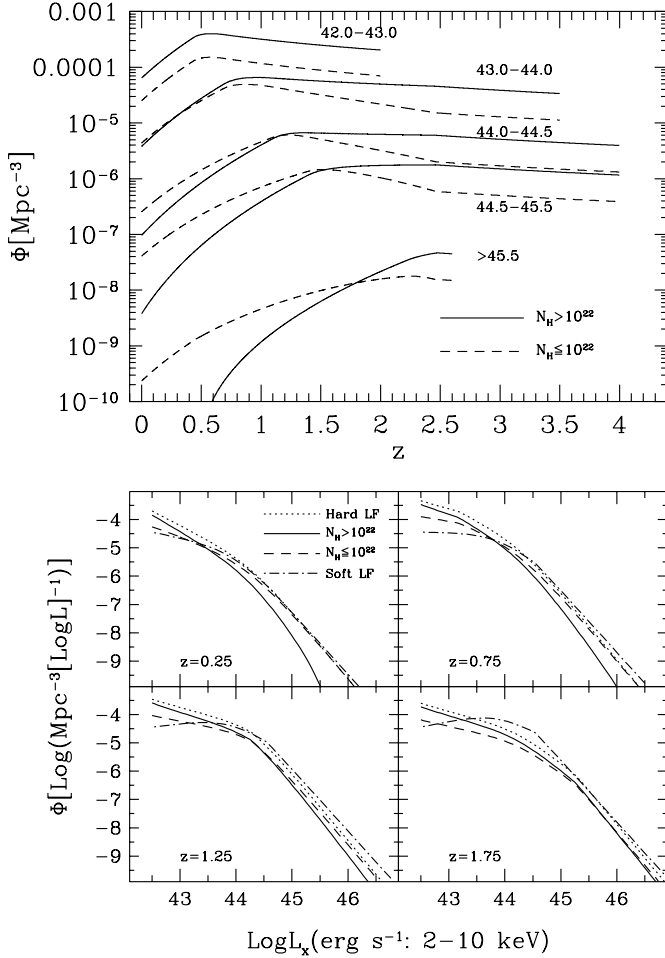


FIG. 17.—*Top*: Density of absorbed and unabsorbed AGNs in luminosity bins as a function of redshift (fit 4). *Bottom*: Density of absorbed and unabsorbed AGNs as a function of luminosity in four redshift intervals (fit 4). The dot-dashed line is the 0.5–2 keV LF of AGNs of Miyaji et al. (2000; plotted assuming $\Gamma = 1.8$).

we note that an increasing ratio between absorbed and unabsorbed AGNs toward high redshifts has already been included in the synthesis models of Pompilio et al. (2000) and Gilli et al. (2001), although with a different prescription for the absorption distribution.

4.5. The Luminosity Function of Absorbed and Unabsorbed AGNs

It is interesting to plot the evolution of absorbed ($N_H > 10^{22}$ cm⁻²) and unabsorbed AGNs, according to our best-fit LDDE solution (fit 4; Fig. 17). As expected, the absorbed AGNs outnumber the unabsorbed ones at low luminosities and high redshifts. In Figure 17 (*bottom*) the HXLF is compared with the estimate of Miyaji et al. (2000) of the soft X-ray (0.5–2 keV) AGN LF (a slope $\Gamma = 1.8$ has been assumed to convert the 0.5–2 keV luminosities into the 2–10 keV band). It turns out that at low redshifts ($z \sim 0.25$), the soft X-ray LF is almost coincident with our measure of the unabsorbed AGN HXLF, while at high redshifts the soft X-ray LF is consistent, within the uncertainties, with the total HXLF. This behavior is explained by the stronger effects of absorption in soft X-rays than in hard X-rays, especially at low redshifts. As a consequence, at low redshifts, only unabsorbed AGNs are detected in the soft X-ray band, while at high redshifts the bias decreases, and the same population that is

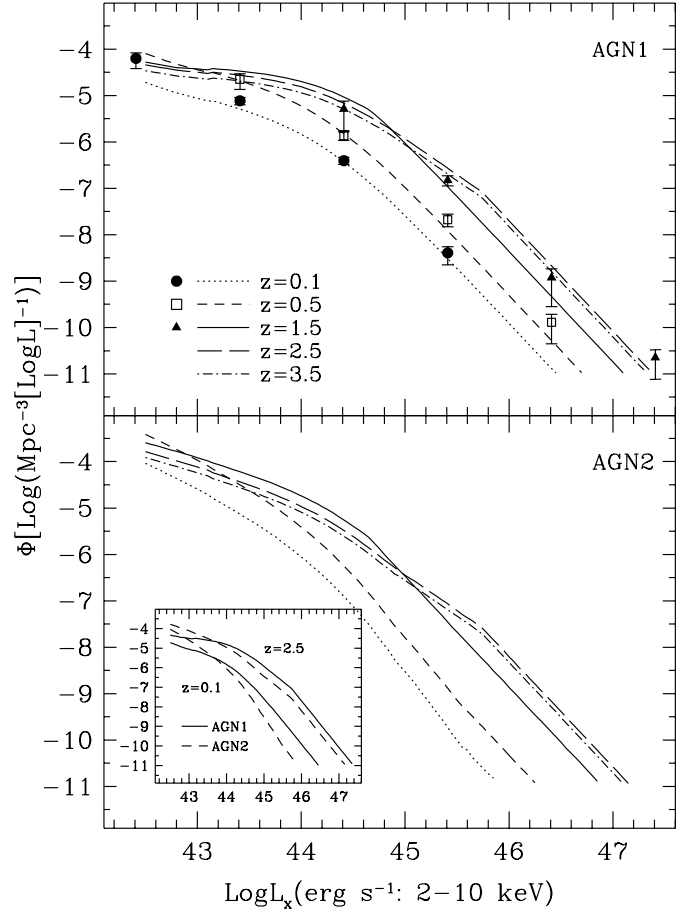


FIG. 18.—*Top*: Evolution of the luminosity function of AGN1's up to $z = 3.5$. The data are the estimates of the density of AGN1's from La Franca et al. (2002). *Bottom*: Evolution of the luminosity function of AGN2's up to $z = 3.5$. The lines have the same meaning as in the top panel. The inset shows the difference among the luminosity functions of AGN1's and AGN2's at $z = 0.1$ and 2.5.

observed in the 2–10 keV band is detected. As a consequence, the soft X-ray LF faces a stronger (LDDE) evolution than that observed for the HXLF (see Hasinger et al. 2005).

4.6. The LF of AGN1's and AGN2's

The space density and evolution of AGN1's and AGN2's can be estimated using the above-described method. In order to correct for the spectroscopic incompleteness of the faint samples, we had to compute the completeness function $g(L_X, z, N_H, R)$ (see § 3.3), which is based on the estimate of the probability of an AGN appearing as an AGN1 as a function of L_X , N_H , and z : $Q1(L_X, z, N_H)$ (shown in Fig. 5). With this estimate in hand (and keeping in mind the uncertainties on the AGN1-AGN2 optical classification discussed in § 3.3), we can derive the AGN1 luminosity function:

$$\Phi_1(L_X, z) = \int \Phi(L_X, z) f(L_X, z; N_H) Q1(L_X, N_H, z) dN_H, \quad (14)$$

where, as discussed in § 3.4, $f(L_X, z; N_H)$ is the N_H distribution. The AGN2 density can be derived by substituting, in the above formula (eq. [14]), $Q1(L_X, N_H, z)$ with $1 - Q1(L_X, N_H, z)$. As can be seen in Figure 18, at low redshifts ($z < 0.5$), the AGN2 density at low luminosities ($L_X \sim 10^{42} - 10^{43}$ erg s⁻¹) is about 5 times larger than that of AGN1's, while the latter outnumber the former

by an order of magnitude at high luminosities ($L_X \sim 10^{46}$). In Figure 18 the AGN1 density in the 2–10 keV band from the *BeppoSAX* High Energy Large Area Survey (HELLAS) as computed by La Franca et al. (2002) is reported. Our estimate of the AGN1 luminosity function is consistent, within the uncertainties, with the La Franca et al. (2002) findings, thus confirming that Q1 is a reliable measure of the probability of an AGN appearing as an AGN1.

5. DISCUSSION

5.1. Comparison with Previous Results

A specific procedure to correct for the spectroscopic incompleteness of faint X-ray sources that also takes into account the selection effects due to X-ray absorption has allowed us to use a large AGN sample to compute the HXLF. Our results extend those of Cowie et al. (2003) and Barger et al. (2005), for which no correction for X-ray absorption is adopted, and the upper limits to the AGN density are estimated by assigning to the unidentified sources the redshifts corresponding to the centers of each L_X - z bin.

An LDDE model provides the best fit to the HXLF evolution up to $z = 4$, in agreement with the Ueda et al. (2003) findings obtained using a smaller and brighter sample and also with the estimates of Cowie et al. (2003), Fiore et al. (2003), Hasinger et al. (2005), and Silverman et al. (2005), who found that the AGN number density for luminosities lower than $\sim 10^{44}$ ergs s^{-1} peaks at lower redshifts than that of higher luminosity AGNs.

The new result of our analysis concerns the luminosity and redshift dependence of the fraction of absorbed AGNs, which decreases with luminosity and increases with redshift. The luminosity trend had already been pointed out by Ueda et al. (2003; see also Hasinger et al. 2005). In the Ueda et al. (2003) best-fit model the fraction of absorbed AGNs is 57% and 36% at $L_X = 10^{42.5}$ and 10^{45} ergs s^{-1} , respectively. Taking into account only a luminosity dependence on the fraction of absorbed AGNs in our sample (fit 2 in Table 2), the corresponding fractions at $L_X = 10^{42.5}$ and 10^{45} ergs s^{-1} are 68% and 40%, respectively. The two results are remarkably similar, especially if we note that absorbed AGNs with $24 < \log N_H < 25$ are included in our sample but not in Ueda et al. (2003).

The increase of the fraction of absorbed AGNs with redshift, instead, emerges only with our analysis. The difference with respect to the Ueda et al. (2003) findings is due to the larger sample extending to fainter fluxes used in the present analysis. Indeed, if we restrict our analysis to a subsample (fit 5 in Table 2) of 207 objects from the Piccinotti, AMSSn, and CDF-N catalogs and thus quantitatively similar to that used by Ueda et al. (2003), the uncertainties become so large that the redshift dependence is no longer significant while the luminosity dependence is recovered.

It is worth noting that the luminosity and redshift dependence of the absorbed AGN fraction would disappear if one flux-limited sample only were analyzed (as discussed by Perola et al. 2004). A flux-limited sample selects low-luminosity AGNs at low redshifts (which, according to our analysis, are more absorbed) and high-luminosity AGNs at high redshift (which are more absorbed as well!). Then the average fraction of absorbed AGNs turns out to be roughly constant. Only by combining several samples and thus covering wide strips of the L_X - z plane with almost constant redshift or luminosity is it possible to disentangle the true dependencies.

A simple AGN model based on the unified paradigm has been adopted by Treister et al. (2004). Assuming that obscured AGNs outnumber unobscured ones by a factor of 3 without any

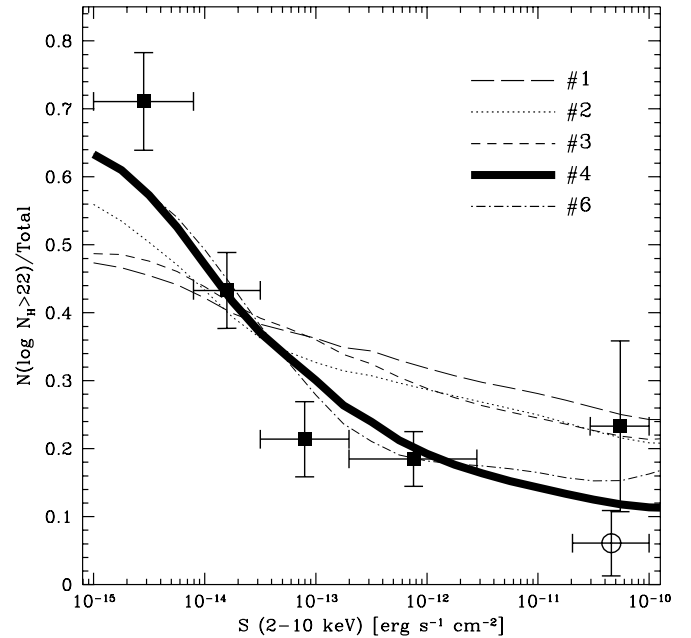


FIG. 19.—Observed fraction of absorbed AGNs as measured from the samples used in this analysis. The lines correspond to the predictions of the fitted HXLF listed in Table 2. The open circle represents the value obtained from the sample of Grossan (1992; not included in the analysis of the HXLF).

luminosity and/or redshift dependence, they claim to be able to reproduce the observed counts and redshift and N_H distributions in the CDF-N and CDF-S samples once all the selection effects are properly taken into account. More recently, Treister & Urry (2005) revised their previous analysis by including a luminosity dependence of the fraction of absorbed AGNs, which appears to provide an equally good fit to several observational constraints. However, in both works, no comparison between the predicted and observed N_H distributions as a function of both L_X and z is made. We have repeated our analysis assuming the Treister & Urry (2005) N_H distribution (see their Fig. 1). Using either the CDF-N plus CDF-S samples only or the full AGN sample used in this work, we found that the only statistically acceptable models were those including a dependence of the fraction of absorbed AGNs as a function of L_X and z , with a behavior similar to what was measured in this paper (see § 4).

The observed and predicted fractions of absorbed ($N_H > 10^{22}/\text{Total}$) AGNs as a function of the observed flux are shown in Figure 19. The open circle is from the Grossan sample (1992; not included in this analysis),¹⁴ and it is plotted in order to show the uncertainties at bright fluxes. As already described by several authors (e.g., Comastri et al. 2001; Tozzi et al. 2005; Perola et al. 2004 and references therein), the average X-ray spectrum significantly hardens toward faint fluxes, and this change is mostly concentrated in the 10^{-14} to 10^{-13} ergs cm^{-2} s^{-1} range, where the fraction of absorbed AGNs rises from about 20% to about 50%. For this reason, this measurement is a very powerful tool for discriminating between different evolutionary scenarios for the N_H distribution. The only acceptable description of the observed ratio between absorbed and unabsorbed AGNs as a function of the hard X-ray flux is obtained only if the ratio depends on *both* luminosity *and* redshift (fits 4 and 6 in Table 2

¹⁴ A proper reassessment of the Grossan sample seems necessary before using it extensively for a detailed statistical analysis. See, e.g., Bianchi et al. (2005) for a discussion on a few sources of the sample.

for LDDE and PLE, respectively). These two models are indistinguishable, and in fact the fraction of absorbed AGNs as a function of the X-ray flux is less sensitive to the shape and evolution of the HXLF than to the evolution of the N_{H} distribution (see also § 3.5).

Recently, Alexander et al. (2005a, 2005b) have found evidence that a fraction of the $z > 1$ submillimeter-emitting galaxies harbor obscured AGNs. They argued that the black holes are almost continuously growing throughout vigorous star formation episodes. These results are in agreement with the hydrodynamical simulation of galaxy mergers by Di Matteo et al. (2005) and Springel et al. (2005), in which the growth of both the black holes and stellar components is taken into account. In this framework, our result of an increase of the fraction of absorbed AGNs with redshift is in agreement with a picture in which the peak epoch of the star formation ($z = 1-2$) corresponds to a heavily obscured rapid black hole phase, which is ultimately preceded by an unobscured quasar phase (Alexander et al. 2005a, 2005b; Hopkins et al. 2005).

5.2. Accretion History of the Universe

Our measure of the HXLF cosmological evolution directly constrains the history of the formation of supermassive black holes (SMBHs) in the galactic centers not only for luminous unobscured AGNs, which can be traced also at longer wavelengths (optical, soft X-rays), but also for the less luminous or obscured AGNs. Starting from our best-fit HXLF it is possible to derive the *intrinsic* (i.e., before absorption) luminosity density in the 2–10 keV band in the universe as a function of redshift:

$$\int L_X \Phi(L_X, z) d \log L_X. \quad (15)$$

This quantity can be converted into the energy density production rate per comoving volume by means of a bolometric correction factor K ($L_{\text{bol}} = K L_X$). The mass inflow rate onto an SMBH, \dot{M}_{BH} , is related to the bolometric luminosity of the AGN, L_{bol} , by $\dot{M}_{\text{BH}} = L_{\text{bol}}(1 - \epsilon)/\epsilon c^2$, where ϵ is the radiative efficiency of the accretion flow (typically taken to be about 0.1; see, e.g., Yu & Tremaine 2002; Marconi et al. 2004; Barger et al. 2005). Once values for ϵ and K are adopted, it is straightforward to derive the accretion rate density as a function of redshift,

$$\dot{\rho}_{\text{BH}}(z) = \frac{1 - \epsilon}{\epsilon c^2} \int K L_X \Phi(L_X, z) d \log L_X, \quad (16)$$

and the total accreted mass, i.e., the total density in massive black holes, if we assume that the initial mass of seed black holes at redshift z_s is negligible with respect to the total mass:

$$\rho_{\text{BH}}(z) = \int_z^{z_s} \dot{\rho}_{\text{BH}}(z) \frac{dt}{dz} dz. \quad (17)$$

In Figure 20 (*top*) we show our direct estimate of the *intrinsic* luminosity density in the 2–10 keV band as a function of redshift from our best-fit HXLF. Assuming $\epsilon = 0.1$ and the luminosity-dependent bolometric correction extensively discussed by Marconi et al. (2004; their eq. [21]), the total density of massive black holes as a function of redshift reported in Figure 20 is obtained by integration of the HXLF starting from $z_s = 4.5$, for $L_X > 10^{41}$ ergs s^{-1} and $N_{\text{H}} < 10^{26}$ cm^{-2} (as explained in § 3.4). The final accreted mass corresponds to a black hole mass density in the local universe of $\rho_{\text{BH}} = 3.2 h_{70}^2 \times 10^5 M_{\odot} \text{Mpc}^{-3}$. A somewhat higher value $\rho_{\text{BH}} = 4.0 h_{70}^2 \times 10^5 M_{\odot} \text{Mpc}^{-3}$ is ob-

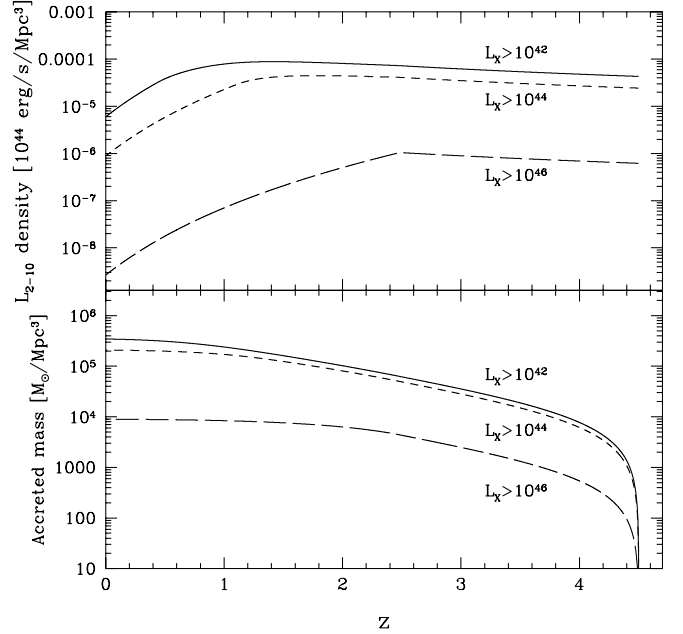


FIG. 20.—*Top*: Intrinsic (before absorption) luminosity density in the 2–10 keV band as a function of redshift from our best-fit HXLF. *Bottom*: Total accreted mass as a function of redshift.

tained for a single-valued bolometric correction factor $K = 40$ (Elvis et al. 1994). These results are consistent, within the errors, with the SMBH density estimate of $\rho_{\text{BH}} = 4.6_{-1.4}^{+1.9} h_{70}^2 \times 10^5$ derived from dynamical studies of local galaxy bulges (see, e.g., Marconi et al. 2004; Ferrarese 2002). As shown in Figure 20, the vast majority of the accretion rate density and black hole mass is produced by the low-luminosity AGNs ($L_X < 10^{44} - 10^{45}$ ergs s^{-1}) down to redshift $z \sim 1$. As already shown by the LDDE model of the HXLF, high-luminosity AGNs are already formed at redshift ~ 2 while low-luminosity AGNs keep forming down to $z \sim 1$. This result is in qualitative agreement with semi-analytical models for galaxy formation and star formation rates, such as those of Balland et al. (2003), Menci et al. (2004), and Granato et al. (2004), or with the hydrodynamical simulations, such as those of Di Matteo et al. (2005), Springel et al. (2005), and Hopkins et al. (2005).

6. CONCLUSIONS

We have devised a method for computing the AGN HXLF that allows us to correct both for the spectroscopic incompleteness of the faint samples and for the selection effects due to the X-ray K -correction. Thanks to this method, we have been able to collect a sample of about 500 AGNs up to $z = 4$. The most important results can be summarized as follows:

1. There is evidence that the fraction of absorbed ($N_{\text{H}} > 10^{22}$ cm^{-2}) AGNs decreases with X-ray luminosity and increases with redshift.
2. The AGN HXLF up to $z = 4$ is best represented by an LDDE model in which the low-luminosity ($L_X \sim 10^{43}$ ergs s^{-1}) AGNs peak at $z \sim 0.7$ while high-luminosity AGNs ($L_X > 10^{45}$ ergs s^{-1}) peak at $z \sim 2$.
3. We can rule out a PLE model on the basis of several arguments that take into account the discrepancies with the optical and hard X-ray LF of AGN1's and the overpredictions of the soft X-ray counts and XRB intensity.
4. We estimate a density of supermassive black holes in the local universe of $\rho_{\text{BH}} = 3.2 h_{70}^2 \times 10^5 M_{\odot} \text{Mpc}^{-3}$, which is

consistent with the recent estimates of local galaxy black hole mass function.

The authors are grateful to the referee for helpful comments and constructive criticism that improved the manuscript. We

acknowledge A. Marconi for useful discussions, G. Hasinger and A. Moretti for providing data in machine-readable format, and P. Tozzi for providing the N_{H} measurements of the sources in the CDF-S sample before publication. This research has been partially supported by ASI, INAF-PRIN 270/2003, and MIUR Cofin-03-02-23 grants.

REFERENCES

- Akiyama, M., et al. 2003, *ApJS*, 148, 275
 Alexander, D. M., Bauer, F. E., Chapman, S. C., Smail, I., Blain, A. W., Brandt, W. N., & Ivison, R. J. 2005a, *ApJ*, 632, 736
 Alexander, D. M., et al. 2003, *AJ*, 126, 539
 ———. 2005b, *Nature*, 434, 738
 Anders, E., & Grevesse, N. 1989, *Geochim. Cosmochim. Acta*, 53, 197
 Antonucci, R. 1993, *ARA&A*, 31, 473
 Baldi, A., Molendi, S., Comastri, A., Fiore, F., Matt, G., & Vignali, C. 2002, *ApJ*, 564, 190
 Balland, C., Devriendt, J. E. G., & Silk, J. 2003, *MNRAS*, 343, 107
 Barger, A. J., Cowie, L. L., Mushotzky, R. F., Yang, Y., Wang, W.-H., Steffen, A. T., & Capak, P. 2005, *AJ*, 129, 578
 Barger, A. J., et al. 2003, *AJ*, 126, 632
 Bauer, F. E., Alexander, D. M., Brandt, W. N., Schneider, D. P., Treister, E., Hornschemeier, A. E., & Garmire, G. P. 2004, *AJ*, 128, 2048
 Bianchi, S., Guainazzi, M., Matt, G., Chiaberge, M., Iwasawa, K., Fiore, F., & Maiolino, R. 2005, *A&A*, 442, 185
 Boyle, B. J., Georgantopoulos, I., Blair, A. J., Stewart, G. C., Griffiths, R. E., Shanks, T., Gunn, K. F., & Almaini, O. 1998, *MNRAS*, 296, 1
 Boyle, B. J., Shanks, T., Croom, S. M., Smith, R. J., Miller, L., Loaring, N., & Heymans, C. 2000, *MNRAS*, 317, 1014
 Brandt, W. N., & Hasinger, G. 2005, *ARA&A*, 43, 827
 Brusa, M., et al. 2003, *A&A*, 409, 65
 Caccianiga, A., et al. 2004, *A&A*, 416, 901
 Cocchia, F., et al. 2005, *A&A*, submitted
 Comastri, A., Fiore, F., Vignali, C., Matt, G., Perola, G. C., & La Franca, F. 2001, *MNRAS*, 327, 781
 Comastri, A., Setti, G., Zamorani, G., & Hasinger, G. 1995, *A&A*, 296, 1
 Cowie, L. L., Barger, A. J., Bautz, M. W., Brandt, W. N., & Garmire, G. P. 2003, *ApJ*, 584, L57
 Croom, S. M., Smith, R. J., Boyle, B. J., Shanks, T., Miller, L., Outram, P. J., & Loaring, N. S. 2004, *MNRAS*, 349, 1397
 De Luca, A., & Molendi, S. 2004, *A&A*, 419, 837
 Di Matteo, T., Springel, V., & Hernquist, L. 2005, *Nature*, 433, 604
 Elvis, M., et al. 1994, *ApJS*, 95, 1
 Fasano, G., & Franceschini, A. 1987, *MNRAS*, 225, 155
 Ferrarese, L. 2002, *ApJ*, 578, 90
 Fiore, F., et al. 2000, *NewA*, 5, 143
 ———. 2003, *A&A*, 409, 79
 Gehrels, N. 1986, *ApJ*, 303, 336
 Georgantopoulos, I., Stewart, G. C., Shanks, T., Boyle, B. J., & Griffiths, R. E. 1996, *MNRAS*, 280, 276
 Giacconi, R., et al. 2002, *ApJS*, 139, 369
 Gilli, R., Risaliti, G., & Salvati, M. 1999, *A&A*, 347, 424
 Gilli, R., Salvati, M., & Hasinger, G. 2001, *A&A*, 366, 407
 Granato, G., De Zotti, G., Silva, L., Bressan, A., & Danese, L. 2004, *ApJ*, 600, 580
 Grossan, B. A. 1992, Ph.D. thesis, MIT
 Halpern, J. P., Eracleous, M., & Forster, K. 1998, *ApJ*, 501, 103
 Hasinger, G. 2003, in *AIP Conf. Proc.* 666, *The Emergence of Cosmic Structure*, ed. S. S. Holt & C. Reynolds (New York: AIP), 227
 Hasinger, G., Miyaji, T., & Schmidt, M. 2005, *A&A*, 441, 417
 Hopkins, P. F., Hernquist, L., Martini, P., Cox, T. J., Robertson, B., Di Matteo, T., & Springel, V. 2005, *ApJ*, 625, L71
 Kinzer, R. L., Jung, G. V., Gruber, D. E., Matteson, J. L., & Peterson, L. E. 1997, *ApJ*, 475, 361
 La Franca, F., & Cristiani, S. 1997, *AJ*, 113, 1517
 La Franca, F., Franceschini, A., Cristiani, S., & Vio, R. 1995, *A&A*, 299, 19
 La Franca, F., et al. 2002, *ApJ*, 570, 100
 Lampton, M., Margon, B., & Bowyer, S. 1976, *ApJ*, 207, 894
 Maccacaro, T., Della Ceca, R., Gioia, I. M., Morris, S. L., Stocke, J. T., & Wolter, A. 1991, *ApJ*, 374, 117
 Mainieri, V., Bergeron, J., Hasinger, G., Lehmann, I., Rosati, P., Schmidt, M., Szokoly, G., & Della Ceca, R. 2002, *A&A*, 393, 425
 Maiolino, R., & Rieke, G. H. 1995, *ApJ*, 454, 95
 Marconi, A., Risaliti, G., Gilli, R., Hunt, L. K., Maiolino, R., & Salvati, M. 2004, *MNRAS*, 351, 169
 Marshall, F. E., Boldt, E. A., Holt, S. S., Miller, R. B., Mushotzky, R. F., Rose, L. A., Rothschild, R. E., & Serlemitsos, P. J. 1980, *ApJ*, 235, 4
 Menci, N., Fiore, F., Perola, G. C., & Cavaliere, A. 2004, *ApJ*, 606, 58
 Mignoli, M., et al. 2004, *A&A*, 418, 827
 Miyaji, T., Hasinger, G., & Schmidt, M. 2000, *A&A*, 353, 25
 Moretti, A., Campana, S., Lazzati, D., & Tagliaferri, G. 2003, *A&A*, 403, 297
 Morrison, R., & McCammon, D. A. 1983, *ApJ*, 270, 119
 Norman, C., et al. 2002, *ApJ*, 571, 218
 Padovani, P., Allen, M. G., Rosati, P., & Walton, N. A. 2004, *A&A*, 424, 545
 Page, M. J., et al. 2003, *Astron. Nachr.*, 324, 101
 Panessa, F., & Bassani, L. 2002, *A&A*, 394, 435
 Perola, G. C., et al. 2004, *A&A*, 421, 491
 Piccinotti, G., Mushotzky, R. F., Boldt, E. A., Holt, S. S., Marshall, F. E., Serlemitsos, P. J., & Shafer, R. A. 1982, *ApJ*, 253, 485
 Pompilio, F., La Franca, F., & Matt, G. 2000, *A&A*, 353, 440
 Ranalli, P., Comastri, A., & Setti, G. 2003, *A&A*, 399, 39
 Revnivtsev, M., Gilfanov, M., Jahoda, K., & Sunyaev, R. 2005, *A&A*, in press (astro-ph/0412304)
 Revnivtsev, M., Gilfanov, M., Sunyaev, R., Jahoda, K., & Markwardt, C. 2003, *A&A*, 411, 329
 Risaliti, G., Maiolino, R., & Salvati, M. 1999, *ApJ*, 522, 157
 Setti, G., & Woltjer, L. 1989, *A&A*, 224, L21
 Silverman, J. S., et al. 2005, *ApJ*, 624, 630
 Springel, V., et al. 2005, *Nature*, 435, 629
 Steffen, A. T., Barger, A. J., Cowie, L. L., Mushotzky, R. F., & Yang, Y. 2003, *ApJ*, 596, L23
 Szokoly, G. P., et al. 2004, *ApJS*, 155, 271
 Tozzi, P., et al. 2005, *A&A*, submitted
 Treister, E., & Urry, C. M. 2005, *ApJ*, 630, 115
 Treister, E., et al. 2004, *ApJ*, 616, 123
 Ueda, Y., Akiyama, M., Ohta, K., & Miyaji, T. 2003, *ApJ*, 598, 886
 Vignati, P., et al. 1999, *A&A*, 349, L57
 Yu, Q., & Tremaine, S. 2002, *MNRAS*, 335, 965
 Zheng, W., et al. 2004, *ApJS*, 155, 73
 Zombeck, M. V. 1990, *Handbook of Space Astronomy and Astrophysics* (Cambridge: Cambridge Univ. Press)